Daytime~~iurnal~~ variation of aerosol indirect effect for warm marine boundary layer clouds in the eastern north Atlantic

Shaoyue Qiu[1], Xue Zheng[1], David Painemal[2,3], Christopher R. Terai[1], and Xiaoli Zhou[4,5]

[1]Atmospheric, Earth and Energy Division, Lawrence Livermore National Laboratory, Livermore, California, USA
[2] Science Directorate, NASA Langley Research Center, Hampton, VA, USA
[3] Analytical Mechanics Associates, Hampton, VA, USA
[4]Chemical Sciences Laboratory, NOAA, Boulder, CO, USA,
[5]Cooperative Institute for Research in Environmental Sciences (CIRES), University of Colorado, Boulder, CO, USA

Correspondence to: Shaoyue Qiu (qiu4@llnl.gov)

Abstract. Warm boundary layer clouds in the Eastern North Atlantic region exhibit significant diurnal variations in cloud properties. However, the diurnal cycle of the aerosol indirect effect (AIE) for these clouds remains poorly understood. This study takes advantage of recent advancements in the spatial resolution of geostationary satellites to explore the daytime variation ~~diurnal cycle~~ of AIE by estimating the cloud susceptibilities to changes in cloud droplet number concentration (N_d). Cloud retrievals for four months of July (2018-2021) from SEVIRI on Meteosat-11 over this region are analyzed. Our results reveal a significant "U-shaped" daytime cycle in susceptibilities of cloud liquid water path (LWP), cloud albedo, and cloud fraction. Clouds are found to be more susceptible to N_d perturbations at noon and less susceptible in the morning and evening. The magnitude and sign of cloud susceptibilities depend heavily on the cloud state defined by cloud LWP and precipitation conditions. Non-precipitating thin clouds account for 44% of all warm boundary layer clouds in July and they contribute the most to the observed ~~diurnal~~ daytime variation. Non-precipitating thick clouds are the least frequent cloud state (10%), they exhibit more negative LWP and albedo susceptibilities compared to thin clouds. Precipitating clouds are the dominant cloud state (46%), but their cloud susceptibilities show minimal variation throughout the day.

We find evidence that the daytime variation ~~diurnal cycle~~ of LWP and albedo susceptibilities for non-precipitating clouds are influenced by a combination of the diurnal transition between non-precipitating thick and thin clouds and the "lagged" cloud responses to N_d perturbations. The daytime variation ~~diurnal cycle~~ in cloud fraction susceptibility for non-precipitating thick clouds can be attributed to the daytime ~~diurnal~~ variation in cloud morphology (e.g., overcast or broken). The dissipation and development of clouds do not adequately explain the observed variation in cloud susceptibilities. Additionally, daytime ~~diurnal~~ variation of cloud susceptibility is primarily driven by variation in the intensity of cloud response rather than the frequency of occurrence of cloud states. Our results imply that

38   polar-orbiting satellites with overpass time at 13:30 local time underestimate daytime mean value of cloud

39   susceptibility, as they observe susceptibility daily minima in the study region.

40
41

1. Introduction

Warm boundary layer clouds, including stratus, stratocumulus, and cumulus clouds, are prevalent over the sub-tropical oceans, account for over 30% of the global annual mean cloud coverage (Warren et al., 1988; Wood, 2012). These clouds have a significant net negative radiative forcing on the surface radiation budget. However, our understanding of the aerosol indirect effect (AIE) on these clouds, particularly the impact of aerosols on cloud amount, brightness, and lifetime, remains a significant source of uncertainty in estimating the radiative forcing from human activities. The AIE plays a critical role in the Earth's radiation budget through its interactions with clouds. It consists of two effects: the Twomey effect, which involves the increase in cloud droplet number from increasing aerosols, and leads to an increase in cloud albedo (α_c) from~~due to~~ smaller droplets when the cloud liquid water path (LWP) is held constant (Twomey, 1977), and the cloud adjustment effect, which encompasses the impact of aerosols on cloud amount, cloud water, and α_c through modulating cloud processes (e.g., Albrecht, 1989; Xue and Feingold, 2006; Chen et al., 2014; Gryspeerdt et al., 2019). ~~The Twomey effect has been well studied and quantified (e.g., Bréon et al., 2003; Feingold et al., 2003; Penner et al.; 2004).~~ The cloud adjustment effect ~~, on the other hand, is~~are highly variable with large uncertainties in signs and magnitudes depending on cloud state, boundary layer, and meteorological conditions among other factors (e.g., Han et al., 2002; Wang et al., 2003; Small et al., 2009; Sato et al, 2018).

Previous studies have made significant progress in identifying different cloud processes and feedback mechanisms to explain the responses of CF, LWP, and α_c to aerosol perturbations (e.g., as summarized in Steven and Feingold, 2009; Fan et al., 2016; Gryspeerdt et al., 2019). The cloud adjustment effect is influenced by two key feedback mechanisms: precipitation suppression, and sedimentation-evaporation-entrainment.

Under clean conditions and for clouds predominantly precipitating, an increase in the cloud droplet number concentration (N_d) and associated decrease in~~s~~ droplet sizes, reduces precipitation ~~efficieney~~efficiency, and decreases water loss from precipitation. Consequently, this promotes an increase in cloudiness and cloud LWP (Albrecht, 1989; Qian et al., 2009; Li et al., 2011; Terai et al., 2012, 2015). For non-precipitating clouds, decreased cloud drop size due to increases in N_d impacts CF and LWP through their impact on the entrainment rate. A decrease in cloud droplet size diminishes the sedimentation rate in clouds, causing an accumulation of cloud water near the cloud top. This increased cloud water in the entrainment zone enhances cloud-top radiative cooling, entrainment rate, and evaporation, resulting in a decrease in CF and cloud LWP (Bretherton et al., 2007; Chen et al., 2014; Toll et al., 2019; Gryspeerdt et al., 2019).

Additionally, the faster evaporation rates from smaller droplets enhance cloud-top cooling, downward motion in clouds, total kinetic energy, and horizontal buoyancy gradient. The processes listed above, in turn, increase evaporation and entrainment rate and, thus, forming a positive feedback loop (Wang et al., 2003; Xue and Feingold, 2006; Small et al., 2009; Toll et al., 2019). Furthermore, among non-precipitating clouds, thick clouds with larger LWP exhibit stronger cloud-top longwave radiative cooling rate and therefore stronger cloud-top entrainment rate (e.g., Sandu et al., 2008, Williams and Igel, 2021). Therefore, the classification of cloud states (e.g., precipitating conditions and thickness) is essential for accurately quantifying the AIE and discerning opposing cloud

78 processes. In this study, we classify cloud states based on the LWP-N_d parameter space, as these variables provide

79 the most informative metrics for cloud susceptibility (Zhang et al., 2022).

80 This study ~~focus~~focuses on the Eastern North Atlantic (ENA) region, where the U.S. Department of Energy

81 (DOE) Atmospheric Radiation Measurement program (ARM) deployed the ground-based user facility at the Azores

82 archipelago (Mather and Voyles, 2013). During the summer over ENA region, warm boundary layer clouds exhibit

83 pronounced diurnal variations in their properties and cloud states. For example, b~~B~~ased on ARM surface radar and

84 lidar observations, the frequency of stratocumulus clouds is highest at night, accompanied by an increase in the

85 fraction of precipitating clouds. Throughout the daytime, both cloud fraction and precipitation fraction experience a

86 slight decrease, followed by an increase after sunset (Remillard et al, 2012). The retrieved cloud microphysical

87 properties from ARM ground-based observations show similar "U-shaped" diurnal variations in cloud LWP, liquid

88 water content, and optical thickness (Dong et al., 2014). Additionally, numerical studies have revealed a distinct

89 diurnal cycle of AIE for marine stratocumulus clouds, attributed to changes in cloud properties~~,~~ and boundary layer

90 thermodynamic conditions ~~, and sea surface temperature~~ (e.g., Sandu et al., 2008, 2009). However, ~~the ARM~~

91 ~~ground-based observation is at a fixed location without a sufficient spatial coverage~~ observational analyses based on

92 the ground-based observations at the ENA site or in-situ measurements from field campaigns are often based on a

93 few cases with limited samples and insufficient spatial coverage (e.g., Liu et al., 2016; Wang et al., 2021; Zheng et

94 al., 2022).~~,~~ T~~t~~here have been few observational studies~~analyses~~ investigating the diurnal cycle of AIE in the ENA

95 region. With recent advancements in the spatial resolution of geostationary satellites, this study aims to investigate

96 the diurnal variation of the AIE in warm boundary layer clouds over the ENA region and gain a better understanding

97 of the underlying mechanisms.

98 Both cloud properties and meteorological conditions have substantial spatiotemporal variability~~ties~~ and

99 distinct diurnal variations. Furthermore, changes in meteorological conditions can in turn influence cloud and

100 aerosol properties. One of the main challenges in understanding the AIE lies in isolating the impacts of the

101 confounding meteorological drivers on clouds and aerosols from AIE on clouds. To address this challenge,

102 Gryspeerdt et al. (2016) proposed the use of N_d as an intermediary variable for AIE, instead of using aerosol optical

103 depth (AOD) or aerosol index. The use of N_d circumvents the well-known dependency of AOD on CF and surface

104 wind speed, which does not necessarily reflect actual changes in aerosol loading. Moreover, the control of relative

105 humidity and aerosol type on AOD prevents to establish a direct link between AOD and aerosol concentration or

106 cloud condensation nuclei (CCN).

107 Another common method to disentangle meteorological impacts is to sort the controlling meteorological

108 factors of cloud state, such as relative humidity, lower tropospheric stability, vertical velocity, and examine the AIE

109 accordingly (e.g., Chen et al., 2014; Gryspeerdt et al., 2019). However, this approach overlooks important

110 information, including the frequency of occurrence of specific environmental conditions, the spatiotemporal co-

111 variation of meteorological factors, and the correlations among them. Zhou et al. (2021) and Zhang et al. (2022)

112 proposed a new method ~~aspect t~~to estimate the cloud susceptibility within a confined space (e.g., a 1° × 1° or

113 2° × 2° grid box) of each satellite snapshot by assuming consistent meteorological conditions within this spatial

114 domain. Additionally, it is important to note that meteorological conditions influence albedo susceptibility by

altering the frequency of occurrence of different cloud states (e.g., precipitating and non-precipitating). Specifically, within a particular cloud state, meteorological conditions offer limited information regarding cloud susceptibility (Zhang et al, 2022).

The second main source of uncertainty in observational AIE studies arise from inferring processes in a temporally evolving system based on snapshots of observations (Mülmenstädt and Feingold, 2018). Due to the limited temporal or spatial resolution of the observations, most studies assume a Markovian system, where clouds and AIE are assumed to only relate to the current state of the system and have no memory of the past states. However, this assumption contradicts the nature of the cloud system. As found by model simulations and observations, theObservational and modeling studies have shown that aerosol-cloud interaction processes take hours to reach the equilibrium state and the sensitivity of AIE is time dependent. Recent advancements in the spatiotemporal resolutions of the geostationary satellite offer an opportunity to address this issue. For instance, using Gaussian-process emulation, Glassmeier et al. (2021) usedapplied a Gaussian-process emulation and derived the adjustment equilibration timescale for LWP to be ~20 hours. to find found that the LWP adjustment for non-precipitating clouds takes ~20 hours to reach the equilibrium state. By satellite observations By tracking the ship tracks in satellite observations along its source emission location in satellite observations, Gryspeeperd et al. (2021) quantified the timescalefound a similar AIE timescale of AIE ofto be ~20 hours or longer and the magnitude of LWP susceptibility increases with time. In addition, By tracking cloud systems in satellite observations, Christensen et al. (2020) founddiscovered that influence of aerosols on cloud LWP, CF, and cloud top height persists two to three days by tracking cloud systems in satellite observations. To concludeIn summary, the sensitivity of cloud responses to N_d perturbations changes with time and, thus, the assumption that AIE has no memory of its past state likely failsis inadequate. Christensen et al. (2020) tracked the influence of aerosols on cloud lifetime and development at different cloud stages, and Gryspeerd et al. (2021) quantified the timescale of aerosols' impact on CF and LWP. Nonetheless, the direct evaluation of the impact of cloud memory on the quantified cloud susceptibility remains unexplored, to the best of our knowledge.

To facilitate a process-level understanding of the drivers behind the diurnal variation of AIE for warm boundary layer clouds, we will classify warm boundary layerthese clouds into three states: precipitating clouds, non-precipitating thick clouds, and non-precipitating thin clouds. We investigate the changes in both the frequency of occurrence of cloud states and the magnitude intensity of AIE for different cloud states throughout the day. Additionally, we track document the temporal changes in cloud state within each fixed 1° × 1° grid box and quantify the influences of cloud memory and state transition on AIE. Section 2 describes the datasets as well as the methodology employed to quantify cloud susceptibilities, distinguish precipitating clouds from the satellite retrievals, and track cloud states. We present our results in Section 3. Section 3.1 characterizes the general conditions of warm boundary clouds over the ENA region during the summer. Section 3.2 introduces the LWP-N_d parameter space and illustrates the dependence of cloud responses to N_d perturbations on cloud states. We then, discuss the mean daytime diurnal variation of cloud susceptibilities for all cloud states in Section 3.3, followed by an analysis ofin the AIE diurnaldaytime variation of AIE for each cloud state and the impact of the state transition on AIE in Section 3.4. In Section 3.5, we decompose the contributions to the daytimediurnal variation of cloud

152 susceptibility into two components, one is from changes in the frequency of occurrence of different cloud states and

153 the other is from changes in the intensity of AIE during the day. Section 4 includes discussions on the similarities

154 and differences in findings between this study and previous studies of AIE and Section 5 is the summary and

155 conclusions of this study.

156 **2. Dataset and Methodology**

157 We use cloud retrievals derived from the Spinning Enhanced Visible InfraRed Imager (SEVIRI) on

158 Meteosat-11, with a spatial resolution of 3 km at nadir and a half-hourly temporal resolution over the ENA region

159 (33-43°N, 23-33°W). SEVIRI cloud products are derived using the Satellite ClOud and Radiation Property retrieval

160 System (SatCORPS) algorithms (e.g., Painemal et al., 2021), based on the methods applied by the Clouds and the

161 Earth's Radiant Energy System (CERES) project, and specifically tailored to support the ARM program over the

162 ARM ground-based observation sites (Minnis et al. 2011, 2020). Given the purpose of this study on quantifying the

163 AIE on warm boundary layer clouds, we focus on four months of July (2018-2021), a period that coincides with the

164 highest frequency of occurrence of warm boundary layer clouds over the ARM ENA site (Rémillard et al. 2012;

165 Dong et al., 2014, 2023).

166 The cloud mask algorithm implemented in SatCORPS is described in Trepte et al. (2019). SatCORPS cloud

167 properties are based on the shortwave-infrared split-window technique during daytime (VISST, Minnis et al. 2011,

168 2020), with cloud optical depth (τ) and effective radius (r_e) being derived using an iterative process that combines

169 reflectance and brightness temperatures from the 0.64 μm and 3.9 μm channels. Cloud LWP is computed from τ and

170 r_e using the formula $LWP = \frac{4 r_e \tau}{3 Q_{ext}}$, where Q_{ext} represents the extinction efficiency and assumed constant of 2.0

171 (Minnis et al. 2011, 2020). The top-of- atmosphere (TOA) broadband shortwave α_c is derived from an empirical

172 radiance-to-broadband conversion using the satellite imager's visible channel and CERES Single Scanning Footprint

173 (SSF) shortwave fluxes, and dependent on solar zenith angle and surface type (Minnis et al. 2016). Cloud top height

174 computations follows the methodology in Sun-Mack et al. (2014).

175 To validate the Meteosat-11 retrieved cloud mask and the detection of boundary layer clouds, we compare

176 the boundary layer cloud fractions derived from Meteosat-11 with the ground-based observations at the ARM ENA

177 site. As seen in Fig. S1, both the diurnal variation and the mean CF of Meteosat-11 agree well with ARM

178 observations. More details on the methodology for the evaluation study are included in the supplementary material.

179 Our analysis focuses on warm boundary layer clouds with cloud tops below 3km and a liquid cloud phase.

180 To focus specifically on boundary layer cloud cases without including the edges of deep clouds, we apply a stricter

181 threshold than merely using the pixel-level cloud top height. We define boundary layer clouds as those with 90% of

182 their cloud tops below 3km, labeling all contiguous cloudy pixels as distinct cloud objects.

183 Cloud N_d is retrieved based on the adiabatic assumptions for warm boundary layer clouds, as in Grosvenor

184 et al. (2018) according to the following equation:

$$N_d = \frac{\sqrt{5}}{2\pi k} \left(\frac{f_{ad} c_w \tau}{Q_{ext} \rho_w r_e^5} \right)^{1/2} \qquad (1)$$

186 In Equation (1), k represents the ratio between the volume mean radius and r_e, assumed to be constant of 0.8 for

187 stratocumulus; f_{ad} is the adiabatic fraction of the observed liquid water path and assumed to be 0.8 for

188 stratocumulus clouds (Brenguier et al., 2011; Zuidema et al., 2012); c_w is the condensation rate, which is a function

189 of ~~cloud~~ temperature and pressure; Q_{ext} is the extinction coefficient, approximated as 2 in this study; and ρ_w is the

190 density of liquid water. While the different components of Eq. (1) could contribute to the uncertainties in N_d, errors

191 in r_e are the dominant drivers in Eq. (1) (Grosvenor et al., 2018).

192 To minimize uncertainties associated with bias in satellite cloud microphysical retrievals, we only select

193 pixels with a minimum r_e of $3\mu m$, a minimum τ of 3, and a solar zenith angle (SZA) of less than 65° (e.g., Painemal

194 et al., 2013; Painemal, 2018; Zhang et al., 2022). The SZA threshold of 65° was chosen to minimize biases observed

195 at high solar zenith angle in r_e and τ (e.g., Grosvenor & Wood, 2014; Grosvenor et al., 2018).

196 In addition, to reduce ~~the~~ uncertainties associated with the adiabatic assumption in the N_d retrieval, we

197 implement a filtering process. For each cloud, we exclude cloudy pixels at the cloud edge, defined as those adjacent

198 to ~~a~~ cloud-free pixels, following a similar sampling strategy suggested by Gryspeerdt et al. (2022). Therefore, all

199 cloud properties in this study refer to the properties of cloud body without cloud edge. It is worthy of note that

200 shallow cumulus clouds with diameters smaller than 9km are not included. The removal of cloud-edge pixels

201 accounts for ~14% of the cloudy pixels. Furthermore, we removed grid boxes containing islands due to the

202 uncertainties in Meteosat retrievals over contrasting underlying surface ~~(not shown)~~. Lastly, to avoid unrealistically

203 large retrievals, we eliminate pixels with the retrieved N_d values exceeding 1000 cm^{-3}, which constituted only

204 0.002% of the data.

205 Cloud susceptibility is quantified as the slope~~s~~ between cloud properties and N_d using a least-square

206 regression. As found by Arola et al. (2022) and~~,~~ Zhou and Feingold (2023), the retrieved cloud susceptibilities are

207 sensitive to small-scale cloud heterogeneity, the co-variability between cloud properties and N_d, and the spatial scale

208 of cloud organization. To ~~smooth the noise~~reduce ~~the~~ biases resulting from ~~the~~ heterogeneity and co-variability, ~~To~~

209 ~~facilitate the analysis,~~ we ~~first~~ first average the 3-km pixel-level cloud retrievals and N_d (Eq. 1) to a regular

210 0.25° × 0.25° grid for each half-hourly time step. ~~As suggested by Feingold et al (2022), N_d retrieval was~~

211 ~~performed at pixel-level using Eq. (1), and then averaged to a 0.25° resolution. This grid averaging process helps to~~

212 ~~eliminate spatial correlations arising from small-scale cloud processes and reduces the influence of extreme values~~

213 ~~on the regression slopes.~~

214 To further mitigate the impact from ~~spatial and temporal~~ co-variability ~~between~~of cloud properties and N_d

215 at larger spatiotemporal scales~~on the derived relationships~~, cloud susceptibility is estimated within a 1° × 1° grid

216 box at each satellite time step (e.g., ~~Zhou et al., 2021;~~ Zhang et al, 2022). ~~Besides the co-variability~~Moreover,

217 ~~c~~Estimating the cloud susceptibility over a confined space also help to constrain the meteorological impacts on AIE,

218 with the assumption of a homogeneous meteorological condition within this spatial scale. Next, susceptibilities are

219 calculated using the 0.25° smoothed data if the number of data points within the 1° × 1° box exceeds six (from a

220 maximum of 16 data points). It is important to note that when computing the 0.25° × 0.25° averaged ~~the mean c~~

221 ~~cloud~~cloud properties ~~at the 0.25° resolution~~, only data from cloudy pixels are used to ensure that the estimated

222 susceptibility is not weighted by CF or impacted by satellite artifacts. Lastly, due to the minimal spatial variability

223 of cloud susceptibility in the study region, the 1° cloud susceptibility is averaged over the study region (33-43°N,

224 23-33°W) to characterize the ~~diurnal~~ daytime variation of AIE. Additionally, results and conclusions of this study

225 are not sensitive to the size of the box calculating the cloud susceptibility (e.g., over a $0.8° \times 0.8°$ box or over a

226 $1.5° \times 1.5°$ box, not shown).

227 Because of the nonlinear relationships between LWP and N_d, the LWP susceptibility is defined as the slope

228 in logarithmic scale, that is: ~~of the log-log regressions~~ $dln(LWP)/dln(N_d)$ (e.g., Gryspeerdt et al. 2019). The

229 albedo susceptibility is estimated as the slope ~~of change in~~ between α_c ~~with~~ and ln (N_d) ~~N_d,~~ equivalent to

230 ~~perturbations as~~ $d\alpha_c/dln(N_d)$ (e.g., Painemal 2018). Lastly, t~~T~~he CF susceptibility is estimated as $dCF/dln(N_d)$.

231 The mean CF is defined as the fraction of cloudy pixels excluding cloud edge to the sum of cloudy and clear pixels

232 within each $0.25° \times 0.25°$ box. Due to the highly variable nature of CF, the variability~~variation~~ in the 0.25° CF

233 could arise ~~may result~~ from quantifying edges or centers of the same cloud layer rather than~~instead of from~~ N_d

234 perturbations. To assess~~test~~ the potential influence of cloud morphology~~geometry~~ on the retrieved CF susceptibility,

235 we excluded ~~removed~~ any $1° \times 1°$ ~~grid box~~scene meeting the following three criteria: ~~with variation in the~~1) the

236 difference between the maximum and minimum 0.25° CF greater than 0.9, 2) ~~while~~the variation in the 0.25° N_d

237 less than 60 cm^{-3}, and 3) the 0.25° CF in the $1° \times 1°$ ~~1°~~box sample the same cloud. The 0.9 and 60 cm^{-3}

238 thresholds represent ~45% of the data. With the three thresholds combined, a~~A~~ total of 17,000 scenes were removed,

239 which accounts for ~24% of the total samples. Removing these scenes does not change the conclusions of CF

240 susceptibility in this study (not shown), which demonstrates that cloud morphology,~~geometry~~ has minimal impact on

241 the retrieved CF susceptibility. Furthermore, as we removed N_d retrievals at cloud edge where N_d likely suffers

242 large uncertainties,~~,~~ ~~and~~cloudy pixels at cloud edge are set as clear for consistency in the calculation of the CF

243 susceptibility. Removing the cloud edge decreases the four-month mean CF for warm boundary layer clouds from

244 21.6% to 19.0%.

245 The susceptibility of the shortwave radiative fluxes to N_d (F_0) is estimated as the sensitivity of the TOA

246 shortwave upward radiative flux (SW_{TOA}^{up}) to N_d perturbations (e.g., Chen et al. 2014; Painemal 2018; Zhang et al.

247 2022). The mean SW_{TOA}^{up} over a $1° \times 1°$ grid box is estimated using Eq. (2), with the assumption that the clear-sky

248 albedo over the ocean is small compared to the cloud albedo:

249
$$\overline{SW_{TOA}^{up}} = \overline{SW_{TOA}^{dn}} \cdot \overline{\alpha_c} \cdot \overline{CF}, \tag{2}$$

250 where SW_{TOA}^{dn} is the grid-box mean TOA shortwave downward radiative flux, which is estimated based on the

251 latitude, longitude, date, and overpass time of each pixel, α_c and CF are the grid-box mean values. Then, F_0 is

252 estimated using the calculated α_c and CF susceptibilities, and the $1° \times 1°$ grid-box mean cloud properties as shown

253 in the equation below:

254
$$F_0 = -\frac{dSW_{TOA}^{up}}{dln(N_d)} = -\overline{SW_{TOA}^{dn}} \cdot \left(\frac{d\alpha_c}{dln(N_d)} \cdot \overline{CF} + \frac{dCF}{dln(N_d)} \cdot \overline{\alpha_c}\right). \tag{3}$$

255 F_0 is in the unit of $W\ m^{-2}\ ln\ (N_d)^{-1}$, and a positive value indicates a decrease in the SW_{TOA}^{up}, which is a *warming*

256 effect at~~to~~ the surface.

257 To minimize uncertainties in the linear regression for the estimated susceptibility, we analyze regressions

258 that exhibited a goodness of fit exceeding the 95% confidence interval (i.e., $\chi^2 < \chi_{0.95,c}^2$), and an absolute

259 correlation coefficient greater than 0.2 (e.g., Painemal, 2018; Zhang et al., 2022). There is a total of ~~119~~5,000

260 samples of the 1° cloud susceptibilities in this study, applying the goodness of fit thresholds result in ~~an~~ exclusions

261 of ~ 33,000- 43,000 ~~262,5000~~ samples for different susceptibilities, which are~~is~~ ~2~~8~~-37~~3~~% of the data. Sensitivity

262 test shows that including cases that fail the goodness of fit test will not change the results and conclusions of this

263 study (not shown). ~~S~~More ~~s~~pecifically, including these cases decrease the magnitude of cloud susceptibilities for all

264 three cloud states, but the signs of cloud responses to N_d perturbations remain consistent.

265   Since precipitating and non-precipitating clouds exhibit distinct responses to aerosol perturbations due to

266 the effect of precipitation suppression and the wet-scavenging feedback, it is critical to distinguish between these

267 two cloud states when estimating AIE. Previous studies have utilized various methods based on the effective radius

268 threshold (e.g., Gryspeerdt et al., 2019, Toll et al., 2019; Zhang et al., 2022) and the rain rate threshold (e.g., Duong

269 et al., 2011; Terai et al., 2015) from satellite retrievals. In our study, we validate these two methods using the

270 precipitating mask estimated from ground-based observations with a radar reflectivity threshold together with the

271 lidar-defined cloud base at the ARM ENA site (e.g., Wu et al., 2020). The thresholds of r_e >12 μm and r_e >15 μm

272 yield hit rates of 0.79 and 0.73, respectively. However, the false alarm rate is higher for r_e >12 μm (0.21) compared

273 to r_e >15 μm (0.1). Rain rate is computed using the empirical relationships derived from ground-based

274 measurements in Comstock et al. (2004) as $R = 0.0156 \left(LWP/N_d\right)^{1.75}$. Using a threshold of R>0.05 mm/h results

275 in a hit rate of 0.65. Consequently, we use the r_e >15 μm threshold to define precipitating clouds in this study.

276   To investigate the dependences of cloud susceptibility~~AIE~~ on previous cloud states and quantify the

277 influence of cloud memory on the estimated cloud susceptibility, we track ~~opt for tracking~~ the historical cloud state

278 over a 1° × 1° grid box ~~fixed location with time~~for a two-hour period~~., rather than tracking cloud parcels in space~~

279 ~~and time.~~ During the summer in the study region, low wind conditions prevail in the boundary layer, with the mean

280 wind speed being less than 10 m/s for 85% of the time and less than 7 m/s for 60% of the time. Therefore, in most

281 cases, less than half of the clouds exit the grid box within the two hours, allowing us to track the previous cloud state

282 within the same grid box (i.e., from an Eulerian perspective). ~~A two-hour tracking window is used to define changes~~

283 ~~in cloud state over the 1° × 1° grid box. Given the typical boundary layer mean wind speed, horizontal advection~~

284 ~~would have limited impact on cloud state transition. Section 3.4 includes more details and discussions on the~~

285 ~~sensitivity of tracking time and the influence of advection on our classification.~~ The influence of cloud memory is

286 assessed by comparing the cloud susceptibilities of clouds that undergo a transition in cloud state with those that do

287 not experience such a transition. Section 3.4 ~~includes~~provides more details and discussion~~s~~ on the sensitivity of

288 tracking time and the influence of advection on our classification.

289 **3. Results**

290 **3.1 General cloud conditions and mean cloud responses to N_d perturbations**

291   In the ENA region, characterized by dominant Bermuda High with its prevailing ridge and zonal synoptic

292 pattern (Mechem et al., 2018), the summer season gives rise to the annual peak in boundary layer cloud coverage ~~at~~

293 ~~ENA.~~ The monthly mean low-level CF retrieved from Meteosat-11 reaches its maximum of 35% in July, compared

294 to an annual mean of 17% during the four-year study period (not shown). This region represents a typical clean

295 marine condition, situated far from continental influences, which results in a consistently lower N_d compared to

296 polluted marine regions, such as the northeastern (NE) Pacific near California or the northwestern Atlantic near the

297 Gulf of Maine. In July, the mean N_d over the ENA region is 65 cm^{-3} with the lower 5th and upper 95th percentile

298 of 15 and 160 cm^{-3}, respectively. The retrieved N_d values in this study closely align with in-situ measurements

299 from the Aerosol and Cloud Experiments in Eastern North Atlantic (ACE-ENA) field campaign. For instance, the

300 in-situ measured N_d in July 2017 varied from 25 to 150 cm^{-3}, with a mean value of 65 cm^{-3} (e.g., Yeom et al.,

301 2021; Zhang et al., 2021). Moreover, our satellite retrieved N_d exhibits good agreement with retrievals based on

302 ground-based observations at the ARM ENA site (e.g., Dong et al., 2014; Wu et al., 2020) and the MOderate

303 resolution Imaging Spectroradiometer (MODIS, e.g., Bennartz 2007; Bennartz and Rausch 2017).
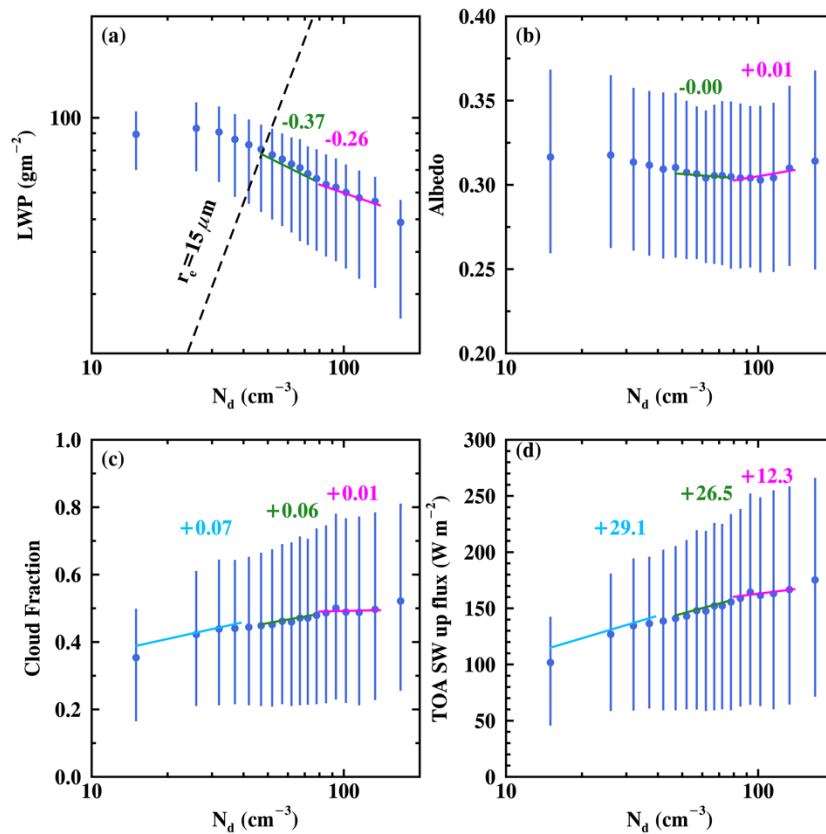
304
305 Figure 1. Relationships between N_d and cloud properties: (a) cloud LWP, (b) cloud albedo, (c) cloud fraction, and
306 (d) TOA shortwave upward radiative flux. The dots represent the mean values, while the whiskers indicate the upper
307 and lower 25th percentile. In (a), the dashed line denotes r_e =15 μm, serving as an indicator of precipitation
308 occurrence, with precipitating clouds located to the left of the line. Blue, green, and magenta lines in panels (a)-(d)
309 represent the regression slopes of the mean cloud properties, and the mean $ln(N_d)$, for $N_d < 40$ cm^{-3}, N_d between
310 40 and 80 cm^{-3}, and $N_d > 80$ cm^{-3}, respectively.
311
312   Previous studies have demonstrated that clouds exhibit diverse responses to aerosol perturbations under

313 clean and polluted conditions (e.g., Fan et al. 2016; Mülmenstädt and Feingold, 2018). Cloud properties derived

314 from satellite retrievals show consistent distinct responses under clean (low) and polluted (high) conditions. Figure

315 1 shows the relationships between the climate mean cloud properties, derived from the pixel-level SEVIRI cloud

10

316 products, and averaged to the $1° \times 1°$ resolution, as a function of the $1° \times 1°$ mean N_d values. To quantify these

317 responses, cloud susceptibility is estimated as the slope of the mean cloud variable changes across N_d bins. In

318 pristine conditions ($N_d < 40\ cm^{-3}$, ~28% of data), clouds predominantly precipitate (r_e >15 μm, Fig. 1a). The mean

319 cloud LWP features a slight increase followed by a decrease with increasing N_d. This result departs from the

320 precipitation suppression hypothesis, in which LWP typically increases. The absence of a precipitation suppression

321 signal is likely attributed to the relatively modest precipitation that ~~witnessed by clouds~~~~occur~~occursed ~~in~~ this

322 region during summer (e.g., Wu et al., 2020; Zheng and Miller, 2022), ~~where the~~ resulting in a minimal ~~effect of~~

323 precipitation suppression effect ~~is minimal~~ and ~~the~~ a dominant entrainment drying effect ~~dominates~~. In terms of α_c,

324 the potential decrease in α_c ~~resulting from~~attributed to a ~~the decreased~~ LWP reduction offsets the potential

325 increases in α_c caused by the Twomey effect, resulting in a net zero change in mean α_c for clouds with $N_d < 40$

326 cm^{-3} (Fig. 1b). Furthermore, the majority of precipitating clouds are broken ~~clouds~~, with ~~the~~ a mean CF that

327 increases with N_d from 0.35 to 0.45 (Fig. 1c). Consequently, the mean SW_{TOA}^{up} flux increases from 100 to 140

328 $W\ m^{-2}$ as N_d increases from 10 to 40 cm^{-3}. This increase in CF for precipitating clouds aligns with previous study

329 over the north Atlantic region across all seasons (e.g., Gryspeerdt et al., 2016). In summary, despite the slight

330 decrease in mean LWP with increasing N_d for precipitating clouds, the mean cloud albedo remains relatively

331 constant, while the mean CF increases, resulting in an overall increase in the TOA reflected shortwave flux ~~by~~

332 ~~clouds~~.

333   Under relatively polluted conditions with $N_d > 40\ cm^{-3}$ (~72% of data), the mean LWP shows a

334 decreasing trend with N_d. For N_d values between 40-80 cm^{-3}, the ln(LWP)- $ln(N_d)$ slope is -0.37~~41~~, while for N_d

335 exceeding 80 cm^{-3}, the slope reaches -0.26~~3~~ (green and magenta lines in Fig. 1a). This negative adjustment of

336 LWP for non-precipitating clouds is consistent with the sedimentation-evaporation-entrainment feedback~~hypothesis~~,

337 as well as with previous studies of stratocumulus clouds in other regions (e.g., Gryspeerdt et al., 2019; Zhang et al.,

338 2022). The mean α_c remains nearly constant within the N_d range of 40-80 cm^{-3} (Fig. 1b). As LWP decreases at a

339 slower rate for N_d >80 cm^{-3}, the Twomey effect becomes more dominant and leads to a slight increase in α_c with a

340 slope of 0.01~~2~~ (magenta line in Fig. 1b). For non-precipitating clouds, the mean CF slightly increases with

341 increasing N_d with a CF susceptibility of 0.06 and 0.01~~3~~ (green and magenta lines in Fig. 1c). As a result, the SW_{TOA}^{up}

342 flux exhibits a weaker susceptibility compared to precipitating clouds (Fig. 1d).

3.2 Daytime mean cloud susceptibilities in the LWP-N_d space

344   One limitation of the relationships derived from the mean cloud properties with sorted N_d is the

345 confounding effect from meteorological impacts on cloud properties and cloud susceptibilities. As a comparison,

346 Fig. 2 shows the mean cloud susceptibility estimated within each half-hourly snapshot's $1° \times 1°$ grid box and

347 averaged in the LWP-N_d parameter space. There are around~~~~ 72~~73~~,000-82,000 samples of the 1° cloud

348 susceptibilities in this study. ~~~~The number of samples for different cloud susceptibilities are slightly different due to

349 the goodness of fit test for each regression. We calculate the mean susceptibilities for LWP-N_d bins with more than

350 100 cloud susceptibility samples. Blank bins in Fig.~~ure~~ 2 are bins with less than 100 samples. ~~~~Figure 2e shows the

351 occurrence frequency of samples for the LWP susceptibility in Fig. 2a.

352   With the assumption that the meteorological condition is homogeneous in each grid box, the estimated

353   cloud susceptibilities exhibit much stronger relationships for all cloud variables compared to the climatological

354   mean adjustment rates shown in Fig. 1. The disparities between the two methods suggest that ~~the~~ meteorological

355   confound~~ersing~~ ~~influences on clouds likely dampen~~tends to obscure the signal of the AIE over the ENA region.

356   Moreover, the cloud responses ~~from both~~ for both precipitating and non-precipitating clouds exhibit consistent signs

357   between the half-hourly (Fig. 2) and climatological-mean approaches (Fig. 1). This consistency is likely attributed to

358   the confined domain (a $10° \times 10°$) and the focus on July in this study, which limit the spatial and temporal

359   covariability between cloud properties and N_d. This consistency also demonstrates that the overall cloud responses

360   to N_d perturbations primarily depend on cloud states (e.g., precipitating conditions and cloud thickness).

361   The dependence of cloud response on cloud state is illustrated in Fig. 2. We define three cloud states: (1)

362   *the precipitating clouds ($r_e > 15$ μm),(2) the non-precipitating thick clouds ($r_e < 15$ μm, LWP > 75 gm^{-2}), and (3)*

363   *the non-precipitating thin clouds ($r_e < 15$ μm, LWP < 75 gm^{-2}), similar to the definition in Zhang et al. (2022).*

364
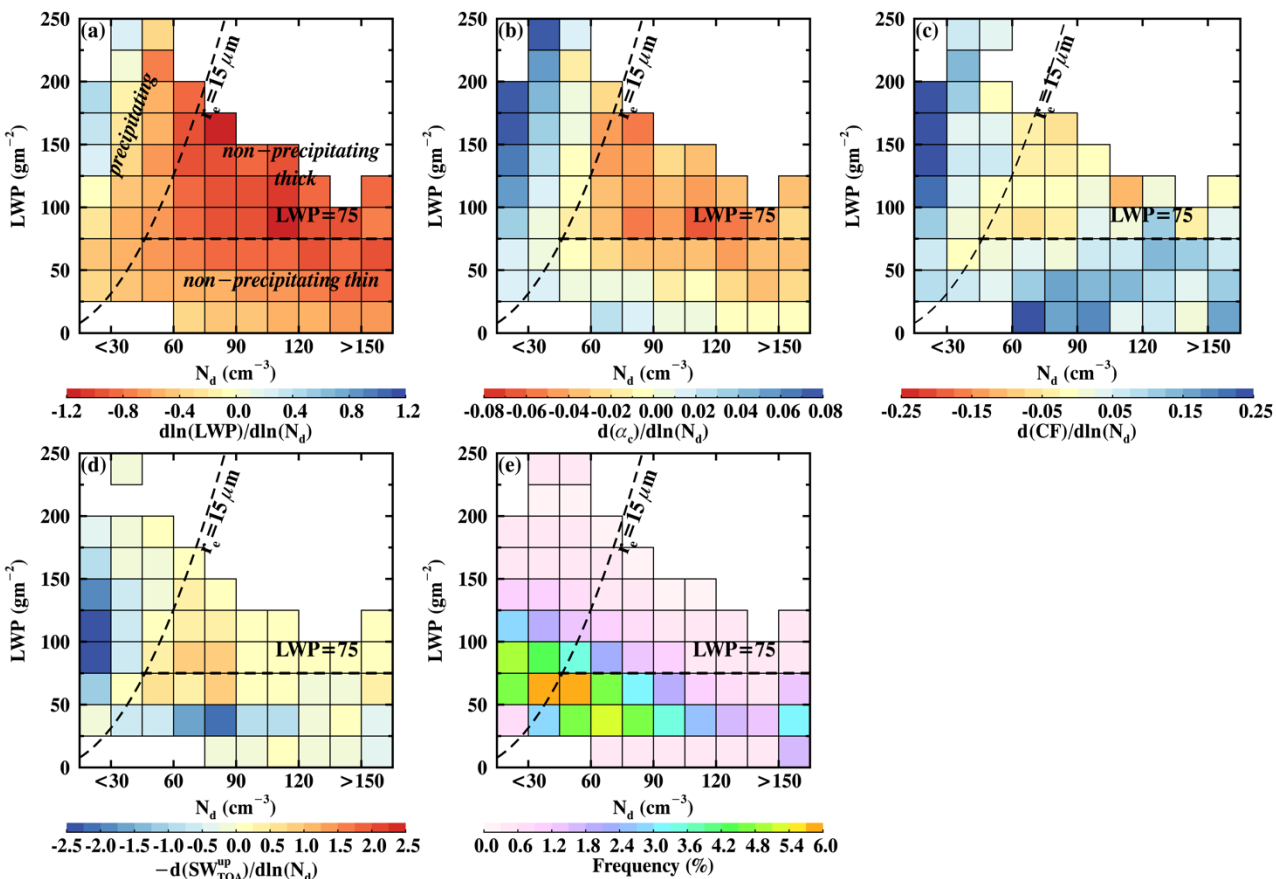
365   Figure 2. Mean cloud susceptibilities for different N_d and LWP bins during the daytime. (a) cloud LWP

366   susceptibility ($dln(LWP)/dln(N_d)$), (b) cloud albedo susceptibility ($d\alpha_c/dln(N_d)$), (c) cloud fraction

367   susceptibility ($dCF/dln(N_d)$), (d) cloud shortwave susceptibility ($-dSW_{TOA}^{up}/dln(N_d)$) weighted by the frequency

368   of occurrence of samples of each bin, and (e) frequency of occurrence of samples in each bin. The dashed lines in

369   (a)-(e) indicate $r_e = 15$ μm and LWP$= 75$ gm^{-2}, as thresholds for precipitation (precipitating clouds located to the

370   left of the line) and thick clouds (with LWP > 75 gm^{-2}). The defined three clouds states are noted in (a).

371   *a.   Precipitating clouds*

372   Among warm boundary layer clouds, precipitating clouds are the dominant cloud state in July over the

373   study region, with a ~~the~~ total frequency of occurrence of~~is~~ 46% (Fig.2e). The increase in cloud LWP with increasing

374   N_d is observed primarily in heavily precipitating thick clouds with $N_d < 30\ cm^{-3}$ and LWP $> 125\ gm^{-2}$ (Fig. 2a).

375   However, these clouds occur relatively infrequently at ENA, accounting for only 2% of the total warm boundary

376   cloud population (Fig. 2e). In contrast, most of the precipitating clouds at ENA are lightly precipitating with

377    $15 < r_e < 20\ \mu m$ (Fig.2e and Fig. S2c) and they exhibit a slight decrease of LWP with N_d (Fig. 2a). The mean LWP

378   susceptibility for lightly precipitating clouds ranges from -0.5 to -0.2 for different bins, with a mean value of -0.4.

379   The standard deviations of LWP susceptibility in different LWP-N_d bins vary between 0.4 to 1.2, while the LWP

380   susceptibilities for precipitating clouds are significantly different than other two cloud states at a 95% confidence

381   level. The slight decrease in LWP for lightly precipitating clouds aligns with previous findings over the Pacific,

382   Atlantic, and global oceans for marine stratocumulus (e.g., Fig S4 in Zhang and Feingold, 2023).

383   The contrasting response of LWP to N_d perturbations for lightly and heavily precipitating clouds can be

384   attributed to the interplay of two competing processes: the depletion of LWP caused by the sedimentation-

385   evaporation-entrainment feedback and the accumulation of LWP resulting from the precipitation suppression

386   feedback. Heavily precipitating clouds are predominantly overcast with a mean CF of 0.65 (Fig. S2a) and a mean r_e

387   of 25 μm (Fig. S2c). Precipitation acts to stabilize the boundary layer, remove water from cloud top, and reduce the

388   entrainment rate (Sandu et al., 2007, 2008). Therefore, heavily precipitating clouds exhibit smaller entrainment rate

389   than non-precipitating clouds with similar LWP. The increase of LWP from precipitating suppression feedback

390   outweighs the decrease of LWP from entrainment feedback and results in a net increase in LWP (e.g., Chen et al.,

391   2014; Toll et al., 2019). ~~Precipitation suppression and entrainment weakening work in concert and result in a net~~

392   ~~increase in LWP with increasing N_d.~~ In lightly precipitating clouds, however, the suppression effect of drizzle on the

393   entrainment rate is minimal. Therefore, the decrease in LWP from entrainment overpowers the increases in LWP

394   from precipitating suppression, leading to a net decrease in LWP with increasing N_d (e.g., Xue and Feingold, 2006).

395   Precipitating clouds generally exhibit brighter cloud albedo with increasing N_d as a result of the weak

396   negative and positive LWP adjustment, particularly in heavily precipitating clouds (Fig. 2b). For lightly precipitating

397   clouds, ~~The~~ α_c susceptibilities range from $-$~~-0.04~~0.02 to 0.07 $ln(N_d)^{-1}$, with a mean of 0.02 $ln(N_d)^{-1}$. The

398   suppression of precipitation by N_d also lead to a significant increase in CF for heavily precipitating clouds, with

399   slopes greater than 0.25 $ln(N_d)^{-1}$ ~~(Fig. 2c)~~. For most of the lightly precipitating clouds, the mean CF exhibits~~have~~

400   small variation with N_d perturbations, with the~~The~~ CF susceptibilities ~~for lightly precipitating clouds show~~

401   ~~variation~~ranging between $\pm 0.025\ ln(N_d)^{-1}$ (Fig. 2c). The standard deviation of the 1° α_c and CF susceptibilities for

402   different precipitating bins ranges between 0.05-0.15 and 0.3-0.6, respectively. The α_c and CF susceptibilities for

403   precipitating clouds are significantly different than other two cloud states at a 95% confidence level. Considering the

404   combined effects of increased α_c and CF, the mean~~total~~ radiative response for precipitating clouds amounts to -13

405    $W\ m^{-2} ln(N_d)^{-1}$, which is a cumulative shortwave susceptibility of bins classified as precipitating clouds in Fig. 2d,

406   weighted by their frequency of occurrence~~a summation of the shortwave susceptibility in Figure 2d for bins~~

407   ~~classified as precipitating clouds~~. The contributions from CF and α_c effects are ~~of~~ -9.5 and $-3.5\ W\ m^{-2}\ ln(N_d)^{-1}$,

408   respectively (Eq. 3).

409   *b. Non-precipitating thick clouds*

410   Non-precipitating thick clouds are less frequent, the total frequency of occurrence is 10% (Fig. 2e). ~~For~~
411   ~~non-precipitating clouds, the~~Their cloud LWP responses ~~of cloud LWP~~ to N_d perturbations differ from that of
412   precipitating clouds. ~~The intensified evaporation from small droplets at high concentrations (e.g., Xue and Feingold,~~
413   ~~2006; Small et al., 2009) and the enhanced entrainment due to large LWP (e.g., Sandu et al., 2008, Williams and~~
414   ~~Igel, 2021) lead to a minimum in LWP susceptibilities of −1.2 at the high-LWP and high- ends (Fig. 2a).~~ The LWP
415   susceptibility for non-precipitating thick clouds is the most negative among the three cloud states, and it reaches a
416   minimum value of -1.2 at the high-LWP and high-N_d ends (Fig. 2a). As LWP and N_d decrease, the LWP
417   susceptibility gradually increases from -1.2 to -0.6~~5~~. This negative susceptibility is likely explained by the
418   evaporation enhancement associated with smaller droplets at high N_d values (e.g., Xue and Feingold, 2006; Small et
419   al., 2009), which works in concert with an entrainment strengthening expected in clouds with large LWP (e.g.,
420   Sandu et al., 2008, Williams and Igel, 2021). The mean LWP susceptibility for non-precipitating thick clouds is
421   -0.94. Consistent with the negative LWP susceptibility, non-precipitating thick clouds become less reflective with
422   increasing N_d for all N_d bins with LWP $> 75\ gm^{-2}$ (Fig. 2b). The mean α_c~~albedo~~ susceptibility is $-0.04\ ln(N_d)^{-1}$.
423   ~~alsotionsfrom~~Due to the enhanced entrainment and evaporation, ~~with increasing N_d,~~ the mean CF mostly~~also~~
424   decreases with increasing N_d, ~~for non-precipitating thick clouds~~ with the mean CF susceptibilities ranging from
425   ~~−0.05 to~~ -0.1 to $+0.04\ ln(N_d)^{-1}$ (Fig. 2c). Considering the decrease in both α_c and CF, non-precipitating thick
426   clouds exhibit a warming effect at~~on~~ the surface, the mean~~total~~ radiative response is $+4.4\ W\ m^{-2}\ ln(N_d)^{-1}$(Fig.
427   2d), with contributions from the albedo effect and the CF effect of 2.9 and 1.5 $W\ m^{-2}\ ln(N_d)^{-1}$, respectively ~~(Fig.~~
428   ~~2d)~~.

429   *c. Non-precipitating thin clouds*

430   Non-precipitating thin clouds are more common than thick clouds during summer, with a total frequency of
431   occurrence of 44% (Fig. 2e). Compared to non-precipitating thick clouds, ~~-~~they exhibit consistent negative but
432   slightly weaker LWP responses to N_d perturbations. The mean LWP susceptibilities range from $-$~~-~~0.9 to $-$~~-~~0.4 in
433   different LWP-N_d bins with~~and~~ a mean of $-$~~-~~0.7 (Fig. 2a). Similar to non-precipitating thick clouds, non-
434   precipitating thin clouds mostly become darker with increasing N_d. Interestingly, with largely decreased LWP, the
435   mean CF mostly increase for all N_d conditions, the CF susceptibilities range from $+0.02$ to $+0.25\ ln(N_d)^{-1}$ (Fig.
436   2c). ~~they exhibit less negative LWP and α_c susceptibilities, but with an opposite increasing trend in CF (Figs. 2b, c).~~
437   ~~The opposite signs in LWP and CF susceptibilities for non-precipitating thin clouds cannot be solely explained by~~
438   ~~the sedimentation- evaporation-entrainment feedback.~~The sedimentation- evaporation-entrainment feedback alone
439   cannot explain the opposite signs in in LWP and CF susceptibilities for non-precipitating thin clouds. A possible
440   explanation for the increased CF is that the enhanced ~~entrainment rate and~~ cloud top radiative cooling rate from
441   aerosol perturbations help to mix the boundary layer, facilitate moisture transport from the ocean surface to cloud,
442   and therefore ~~facilitate~~favor new cloud formation and extend cloud lifetime (e.g., Christensen et al. 2020). This
443   hypothesis is consistent with and supported by the relative low CF for these clouds (Fig. S2a) and the diurnal
444   variation in LWP susceptibility for non-precipitating thin clouds, which will be discussed in the next section. The
445   opposite signs of LWP and CF susceptibilities indicate that the AIE might~~likely~~ redistribute cloud water horizontally

14

446 and make the thin clouds thinner and wider. ~~In the next section, two additional hypotheses regarding the~~
447 ~~development/dissipation of clouds and the transition of cloud states will be tested (Table 1). Due to increases in CF,~~
448 ~~non-precipitating thin clouds have a cooling effect on the surface, with the radiative response of +4.4~~
449 ~~$W\ m^{-2}\ ln(N_d)^{-1}$~~ The CF radiative effect from increased CF dominates the albedo effect from darker clouds and
450 lead a net cooling ~~on~~at the surface. The ~~total~~mean radiative response is $-5.2\ W\ m^{-2}ln(N_d)^{-1}$, with CF and albedo
451 contributions of -8.3 and $+3.1\ W\ m^{-2}ln(N_d)^{-1}$, respectively (Fig. 2d).

452   To sum up, the magnitudes and signs of the responses of cloud LWP, α_c, and CF to N_d perturbations
453 primarily depend on the cloud states. Precipitating clouds mostly become thinner and brighter with increasing N_d,
454 accompanied by ~~an~~a slight increase in CF. An increase in LWP with increasing N_d is observed only for heavily
455 precipitating clouds with $N_d < 30\ cm^{-3}$ and LWP $> 125\ gm^{-2}$. Non-precipitating thick clouds become thinner, less
456 reflective ~~from TOA~~, and decrease in cloudiness with N_d perturbations. On the other hand, non-precipitating thin
457 clouds become ~~slightly~~ thinner and less reflective, but their cloudiness increase as N_d increases. Given the
458 dependence of AIE on cloud state, we will apply the cloud state classification ~~established here will be applied in~~ in
459 the ~~next~~following two sections with the goal of~~to~~ facilitat~~e~~ing a process-level understanding of cloud responses and
460 the daytime~~diurnal~~ variation in cloud susceptibilities.

3.3 Daytime~~Diurnal~~ variation of cloud susceptibility

462   As discussed in the introduction, warm boundary layer clouds exhibit a distinct diurnal cycle in both cloud
463 properties and frequency of occurrence of cloud states during summer. In this section, we investigate the
464 daytime~~diurnal~~ variation of cloud susceptibility from 9 to 18 local standard time (LST) using the half-hourly
465 Meteosat-11 retrievals. The domain mean ~~diurnal~~daytime variation of ~~satellite-based~~ cloud susceptibility is
466 estimated from each half-hourly time step within each $1° \times 1°$ box and then averaged over the study domain (33-
467 43°N, 23-33°W) during the four months. ~~Over~~In the study domain, there is little spatial variability in cloud
468 susceptibilities and the diurnal cycle of the cloud susceptibility ~~over~~for the $1° \times 1°$ box at the ARM ENA site agree
469 well with the domain mean pattern (not shown). Furthermore, diurnal cycle of the cloud microphysical properties
470 (e.g., r_e, τ, LWP, N_d) show little difference between the domain mean value or that averaged over the $1° \times 1°$ box at
471 the ARM ENA site. The cloud microphysics retrievals from Meteosat-11 agree well with retrievals based on ground-
472 based radar and lidar observations in the ~~diurnal~~daytime variation (not shown). Therefore, the ARM ENA site at the
473 Azores archipelago can represent the cloud properties and the AIE for warm boundary layer clouds over the study
474 region.
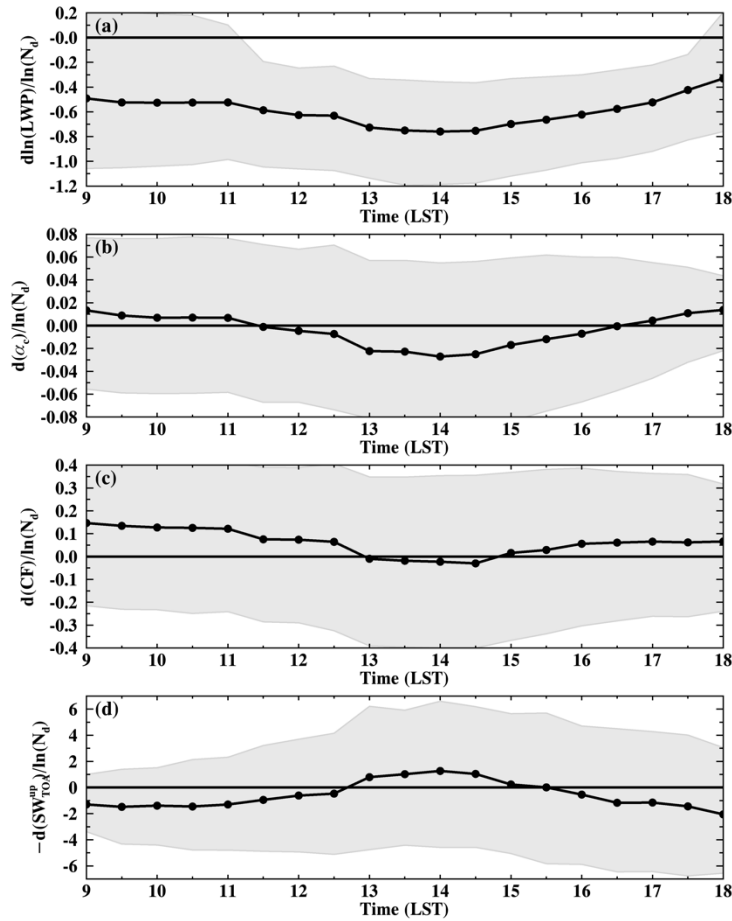
Figure 3. Daytime variation of cloud susceptibilities. (a) cloud LWP susceptibility ($dln(LWP)/dln(N_d)$), (b) cloud albedo susceptibility ($d\alpha_c/dln(N_d)$), (c) cloud fraction susceptibility ($dCF/dln(N_d)$), and (d) cloud shortwave susceptibility ($-dSW_{TOA}^{up}/dln(N_d)$). The shaded areas represent the lower and upper 25th percentile of the cloud susceptibilities for each time step and the solid lines with dots represent the mean values~~the solid lines with symbols represent the mean values. The black solid lines without symbols in (a)-(d) represent the daytime mean values of cloud susceptibilities~~.

Warm boundary layer clouds ~~reveal~~ witness distinct and significant ~~diurnal~~daytime variations in cloud susceptibilities (Fig. 3). For example, the mean LWP susceptibility exhibits a magnitude of change of 0.4 from morning to evening~~noon~~, which corresponds to approximately 30-40% of the overall variability in LWP susceptibility (Fig. 3a). Similarly, the α_c and CF susceptibility undergo magnitude of ~~diurnal~~ changes of approximately 20-30% compared to the overall variability (Figs. 3b and c). The high variability in cloud susceptibility highlights the complex synoptic, meteorological and cloud conditions as well as the interplay between them ~~synoptic conditions that varies diurnally and cloud states~~ in the ENA region. Nevertheless, t~~T~~he ~~diurnal~~daytime variation of cloud susceptibility is statistically significant at a 95% confidence level based on a student's t-test. Interestingly, all three cloud variables exhibit a "U-shaped" diurnal cycle in cloud susceptibilities with less negative/more positive values in the morning and evening and more negative value~~r~~s at noon. Additionally, the α_c and CF susceptibilities switch signs from positive in the morning to negative at noon, and then become

16

494 positive again in the evening. The switch in sign for albedo susceptibility is statistically significant at a 95%
495 confidence level, while the switch in sign for CF susceptibility is not statistically significant. As both α_c and CF
496 increase with increasing N_d in the morning, AIE has a cooling effect ~~on~~ at the surface and the estimated shortwave
497 susceptibility is $-1.4\ W\ m^{-2}\ ln(N_d)^{-1}$. During 13-1$\underline{5}$~~6~~ LST, the shortwave susceptibility switches sign to a
498 warming effect of $+1.2\ W\ m^{-2}\ ln(N_d)^{-1}$ (Fig. 3d).

499   Given the pronounced ~~diurnal~~daytime variation of cloud susceptibility, *how can we explain this distinct*
500 *~~diurnal~~daytime variation, and which state of cloud contributes most to the ~~diurnal~~daytime variation?* One possible
501 explanation is the increased occurrence of precipitating clouds in the morning and evening during summer
502 (Remillard et al, 2012), which increase cloud susceptibility, as depicted in Fig. 2. To investigate this hypothesis and
503 quantify the impacts of different cloud states on the variabilities of cloud susceptibilities, we examined the
504 ~~diurnal~~daytime variation of cloud susceptibility ~~for each cloud state~~, along with the ~~diurnal~~daytime shift in ~~cloud~~
505 ~~state~~ occurrence frequency for each cloud state.

3.4 Daytime~~Diurnal~~ variation of cloud susceptibility for different cloud states

3.4.1 Non-precipitating thin clouds

508   Non-precipitating clouds mainly consist of thin clouds, with a daytime mean occurrence of 44% (Fig. 4a).
509 The highest occurrence ~~of non-precipitating thin clouds~~ is observed around noon, which is consistent with ground-
510 based radar reflectivity measurement at the ENA site (Remillard et al, 2012). Furthermore, as seen in Fig. 4, not
511 only the frequency of cloud occurrence, but also the susceptibilities of LWP, α_c, and CF show distinct
512 ~~diurnal~~daytime fluctuations. For example, the mean LWP susceptibility decreases from -0.4 to -0.9, and the mean
513 α_c susceptibility decreases from 0.02 to $-0.04\ ln(N_d)^{-1}$ from morning to noon, followed by increases in both LWP
514 and α_c susceptibilities in the afternoon. The CF susceptibility is highly positive in the morning and decreases to near
515 zero after 13 LST. In addition, cloud susceptibility for thin clouds in the morning is statistically significantly
516 different from~~than~~ that at noon and in the evening at a 95% confidence level.

517
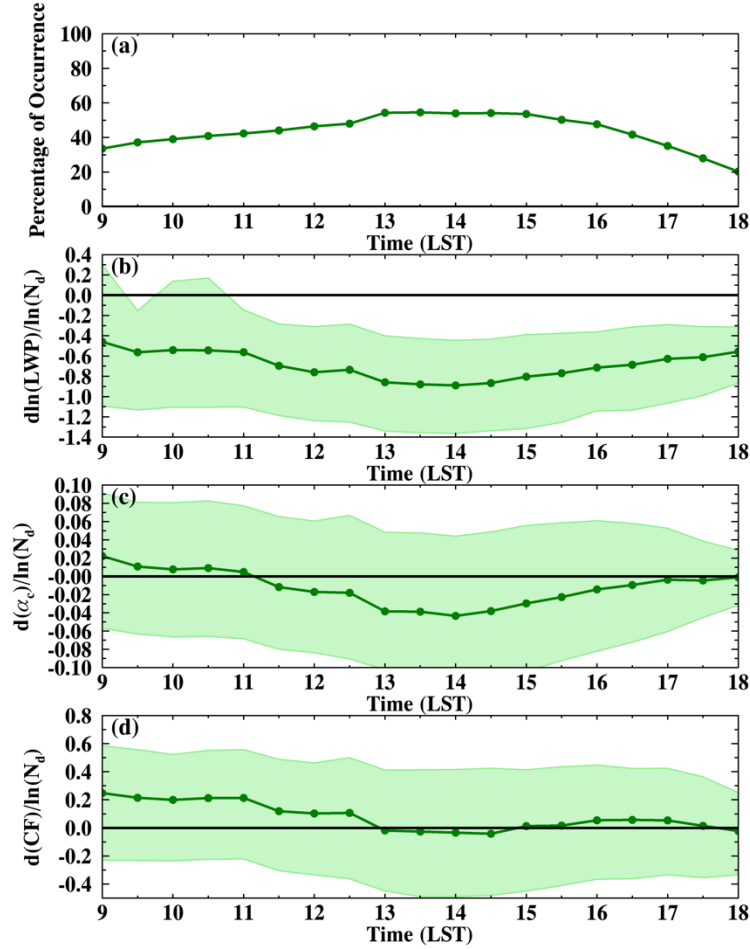
Figure 4. Daytime variation of (a) percentage of occurrence of non-precipitating thin clouds to warm boundary layer clouds, (b) cloud LWP susceptibility ($dln(LWP)/dln(N_d)$), (c) cloud albedo susceptibility ($d\alpha_c/dln(N_d)$), and (d) cloud fraction susceptibility ($dCF/dln(N_d)$) for non-precipitating thin clouds. The shaded areas represent the lower and upper 25th percentile of the cloud susceptibilities for each time step and the solid lines with dots represent the mean values~~and the soli~~. ~~The solid lines without symbols in (a)-(d) represent the daytime mean values~~.

To explain the decrease of cloud susceptibility of non-precipitating thin clouds from morning to noon, we test two hypotheses (H1<u>2</u> and H2<u>3</u> in Table 1). Hypothesis H2<u>3</u> is related to the dissipation of thin clouds during this ~~time period~~period, which is caused by ~~increased solar radiation and~~ <u>a</u> decreased LWP <u>due to increased solar radiation</u>. During the dissipation, ~~if homogeneous mixing dominates,~~ both LWP and r_e decrease. As r_e is raised to the power of $-\frac{5}{2}$ in Eq. (1) compared to τ being raised only to the power of $\frac{1}{2}$, the decreases of LWP and r_e could <u>still</u> result in an increase in the retrieved N_d. <u>Consequently, a</u> ~~The decreased~~ LWP <u>decrease</u> and ~~increased~~ N_d <u>increase</u> lead~~s~~ to a decrease in LWP susceptibility <u>during the dissipation</u> (Gryspeerdt et al., 2019). To examine this hypothesis <u>(H2)</u>, non-precipitating thin clouds are classified as: growing, dissipating, or constant based on the changes in the mean CF, cloud susceptibilities for the three groups are shown in Fig.~~ure~~ ~~S4~~<u>S3</u>. More specifically, we calculate the change in the mean CF within a 30-minute window for each fixed 1° × 1° box. If the mean CF increase (decrease) more than 10%, clouds are classified as growing (dissipating). If the change in CF is less than 10%, clouds are classified as constant. Similar results are obtained using classification methods based on different CF

18

536 thresholds (e.g., from 10% to 30%), and during different time windows from 30-minutes to two hours or changes in
537 the mean LWP (not shown).

538 Table 1. List of hypotheses and associated explanations for the daytime variation of LWP and CF susceptibilities for
539 different cloud states.

-	Cloud state	Hypotheses:	
Daytime evolution of LWP susceptibility	Non-precipitating thin clouds	H1*:	Non-precipitating thick clouds transition to thin clouds from morning to noon, which leads to a daily minimum LWP susceptibility at noon.
		H2*:	Cannot explain. Clouds that are growing or dissipating have similar LWP susceptibilities as clouds with constant CF.
	Non-precipitating thick clouds	H1:	Thin clouds develop to thick clouds from noon to evening, which leads to an increase in LWP susceptibility.
		H2:	Cannot explain.
	Precipitating clouds	H1:	Non-precipitating thin clouds transition to precipitating clouds in the afternoon, which leads to a decrease in LWP susceptibility.
		H2:	Cannot explain.
Daytime evolution of CF susceptibility	Non-precipitating thin clouds	H1:	Thick clouds transitioned to thin clouds from morning to noon, leading to a decrease in CF susceptibility
		H2:	Cannot explain.
	Non-precipitating thick clouds	H1:	Cannot explain.
		H2:	Cannot explain.
		H3*:	Mostly overcast clouds in the morning and evening. CF of overcast clouds is less sensitive to N_d perturbations.
	Precipitating clouds	H1:	Thin clouds transition to precipitating clouds in the afternoon, and lead to a decrease in CF susceptibility
		H2:	Cannot explain.

540 *H1: LWP and CF responses to N_d perturbations slower than the transition of cloud state.
541 *H2: Dissipation or development of clouds.
542 *H3: Changes in cloud morphology.

543

544   As seen in Fig. ures S4S3b, the LWP susceptibilitiesy for non-precipitating thin clouds in the growing or

545 dissipating stages are similar or less negative than clouds that remain constant in CF, which contradicts the

546 hypothesis H2. Additionally, the occurrence of dissipating and developing thin clouds remain relatively constant

547 throughout the day (Fig. S4S3a), which differs from our hypothesis that thin clouds dissipate in the morning.

548 Therefore, the decrease in LWP susceptibility in the morning is *unlikely* to be attributed to the dissipation or

549 development of thin clouds. Yet, due to the observational limitation on estimating the mixing process from satellite

550 retrievals, further investigation is needed to quantify the impact of cloud dissipation and the mixing type on the N_d-

551 LWP relationship.

19

Besides the change in CF, dissipation/development of clouds can be defined by change in LWP. However, as our definition of thin and thick clouds use LWP thresholds, results based on change in LWP are similar to results shown in Fig. 5, but with weaker signal (not shown). This indicates that classification of precipitating verses non-precipitating clouds is necessary in distinguishing cloud responses to N_d perturbations than merely using the LWP threshold.

Hypothesis H12 is related to the response time of cloud LWP and CF to N_d perturbations. Both numerical model simulationsls and observations have shown that the influence of aerosols on cloud LWP, achieved through adjusting the entrainment rate, may take four hours to become apparent and up to 20 hours to reach an equilibrium (Glassmeier et al. 2021; Gryspeerdt et al., 2021). Similarly, the impact of aerosols on CFCF increases gradually from increasing aerosols and may take approximately three to four hours to reach its maximum effect after the initial perturbation (Gryspeerdt et al., 2021). Therefore, we hypothesize that during the diurnal transition of cloud stateif clouds change state during the adjustment time, changes in entrainment rate, LWP responses, as well as CF responses, are slower than the 30-mins resolution of the geostationary satellite and clouds may still retain the "memory" of their susceptibilities from the previous states. The possible physical processes and mechanisms for this hypothesis is that the LWP susceptibility is mainly driven by cloud top evaporation and entrainment rate. The positive feedback among entrainment, evaporative cooling, long-wave radiative cooling, and mixing from cloud top form a positive feedback loop and set up an environment conductive to enhanced entrainment and evaporation. These feedback and environment will not change immediately even when the cloud LWP decrease and cloud transition to a thin state or vice versa. With the diurnal variation in cloud properties and transition in cloud state, resulting init leads to a diurnal variation evolution in cloud susceptibility. This hypothesis is tested in Figure 5.

To quantify the dependence of current cloud susceptibility on previous cloud states, we track the cloud state for each 1° × 1° box backward in time for two hours and classify the non-precipitating thin clouds into three groups (Fig. 5): (1) thin clouds that are currently classified as thin clouds and didn't change states in the past two hours (thin → thin), (2) thin clouds that evolved from precipitating clouds (rain → thin), and (3) thin clouds that decayed from non-precipitating thick clouds (thick → thin). This backward tracking classification is applied at each time step.

As shown in Fig. 5a, at 9 LST, ~50% of the non-precipitating thin clouds originate from thick clouds in previous hours. The transition from thick to thin clouds is likely caused by the increased solar radiation after sunrise, leading to cloud turbulents decoupling from the ocean surface and a decrease in cloud LWP. In the evening, on the other hand, around 80% of the thin clouds are thin clouds in previous hours. In addition, less than 20% of the non-precipitating thin clouds transitionare from precipitating clouds.
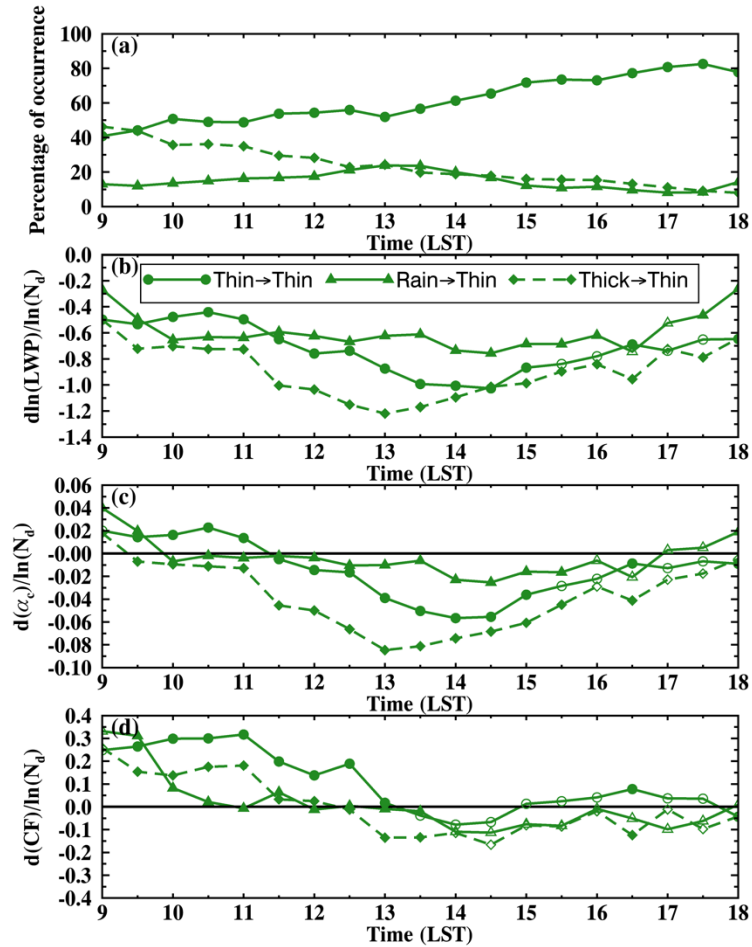
Figure 5. Daytime variation of non-precipitating thin clouds transition from non-precipitating thin clouds (thin → thin, solid line with circle symbols), precipitating clouds (rain → thin, solid line with triangle symbols), and non-precipitating thick clouds (thick → thin, dashed line with diamond symbols) in previous two hours. Symbols for different state transitions are noted in (b). In (b)-(d), filled markers indicate data points that are significantly different from the other two groups (p<0.05), while open markers indicate statistical insignificance.

In consistent with our hypothesis, nNon-precipitating thin clouds that are previously thick have significantly more negative LWP and α_c susceptibilities than thin clouds that are previously thin or precipitating (Figs. 5b and c). This difference is consistent with results shown in Fig. 2 between thick and thin clouds and could be attributed to the enhanced entrainment in the thick clouds. The differences between the two categories are most pronounced from late morning to early afternoon and less pronounced in the early morning and evening. Such pattern is likely attributed to the daytime evolution of marine boundary layer and cloud coupling state. For example, Iin the early morning (e.g., 9-10 LST), even with higher frequency of occurrence of thick clouds transitioning to thin clouds, the LWP susceptibility for the thick-to-thin category is less negative compared to later time (dashed line with diamond symbols in Figs 5a, b). This is attributeddue to the less negative LWP susceptibility for non-precipitating thick clouds in earlier time (e.g., 7-9 LST, not shown), in connection with a well-mixedcoupled boundary layer able to transporting moisture from the ocean to the clouds, which and compensates the moisture loss

from aerosol--enhanced entrainment (e.g., Sandu et al., 2008~~,~~), so that both thick and thin clouds exhibit less negative LWP susceptibilities. From late morning to early afternoon, with deepening of boundary layer and clouds decoupled from surface, LWP susceptibility for thick clouds largely decreases and reaches a daily minimum, which contributes to the largest difference between the thin-to-thin and thick-to-thin categories shown in Fig. 5b. From afternoon to evening, with the increase of LWP susceptibility for non-precipitating thick clouds, and the difference between the two categories is less pronounced.) ~~The differences among the three groups are more pronounced in the morning when a larger portion of thin clouds are decayed from thick clouds. In the afternoon, with less than 10% of thin clouds transitioning from thick or precipitating clouds, the differences among the three groups become less significant.~~ These results support our hypothesis that clouds retain the memory of their responses to N_d perturbations from their previous states.

Similar to LWP~~ly~~, responses of CF to N_d perturbations in the morning retain the memory of the previous state of clouds. As seen in Figure 5d, thin clouds that transitioned from thick clouds or precipitating clouds have significantly less positive CF susceptibility than thin clouds that ~~are~~ were previously thin, particularly in the morning. As the CF susceptibility for thin clouds that ~~transitioned~~evolved from precipitating ~~clouds~~ and thick clouds greatly decrease from morning to noon, the CF susceptibility for thin clouds decrease from large positive to near zero from morning to noon (Fig. 4c). A maximum in CF susceptibility in the early morning is likely associated with the ~~Another possible explanation on the evolution of CF susceptibility is the~~ influence of aerosols on boundary layer mixing and the evolution of boundary layer from morning to noon. The enhanced entrainment rate and radiative cooling rate from N_d perturbations help to destabilize the boundary layer and transport moisture from the ocean surface to clouds, facilitating new cloud formation (e.g., Christensen et al. 2020). As the boundary layer is ~~mostly~~typically well mixed in the morning with clouds coupled to the surface, the~~is~~ impact of aerosols on CF is strongest in the morning and gradually decrease from morning to noon. ~~This is likely due to the less positive CF susceptibility for non-precipitating thick and precipitating clouds in the morning, which will be discussed in section 3.4.2 and 3.4.3.~~ In the afternoon, ~~on the other hand,~~ thin clouds transition from all three states have near-zero CF responses to N_d perturbations. Further analyses and model simulations are needed to better understand aerosols' impact and the associated diurnal evolution of entrainment rate, boundary layer mixing, cloud cover and lifetime to explain the observed daytime variation of CF susceptibility for non-precipitating thin clouds.

The impact of the cloud memory of AIE on current cloud susceptibility is also evident within a 30-minute window when a transition of cloud state just occurs (Fig. ~~S5~~S4). Consistent with the findings in Fig~~ure~~ 5, thin clouds that transition from thick clouds exhibit much more negative LWP and α_c susceptibilities compared to thin clouds that remain thin during the 30 minutes. ~~However, due to the limited~~ Yet, the number of cases experiencing a transition in cloud state within a 30-miniute window is limited (Fig. ~~S5~~S4a).~~, the differences in cloud susceptibilities between thin cloud undergoing a change in cloud states and those that do not are statistically insignificant after 14 LST.~~ In addition, the impact of the transition in cloud state on the current cloud susceptibility persists for at least four hours (Fig. ~~S6~~S5). As ~~It is important to note that o~~our tracking method does not follow individual cloud parcels to track changes in their states, ~~and~~ the influence of cloud advection may become ~~more~~ significant over longer tracking time, such as four hours. Therefore, a two-hour tracking window is used in this study.

639   As discussed in the method section, while the advective effects in our study are expected to be modest, we
640 further isolate their impact, by performing an analysis for cloud scenes with wind speed of less than 7 m/s (60% of
641 time), when clouds are somewhat stationary in two hours. Influence of transition in cloud state is consistent as in
642 Fig. 5 with more negative LWP and α_c susceptibilities for thin clouds transitioned from thick clouds, while the
643 signal is slightly stronger (not shown). To further isolate test the influence of cloud advection fromon the tracked
644 transition of cloud state and cloud susceptibilities, we focus on low wind conditions with wind speed of less than
645 7m/s, when cloudss are considered stationary during the two-hour period (60% time). The influence of cloud state
646 transition on cloud susceptibility is stronger with larger differences in LWP and α_c susceptibilities between clouds
647 experiencinged transition in cloud state thanwith clouds that did not (not shown). Therefore, is consistency confirms
648 that we believe our tracking method can extractcapture the signal of cloud state transition and and its impact on
649 cloud susceptibilities during summer in theis study region.
650   In summary, the "U-shaped" diurnaldaytime variations in LWP and α_c susceptibilities for non-precipitating
651 thin clouds are likely due to a combined effect of the transition in cloud state and cloud retaining the memory of AIE
652 of their previous state. From morning to noon, as non-precipitating thick clouds transition evolve to thin clouds, they
653 retain their memory of the large negative LWP susceptibility. Therefore, both LWP and α_c susceptibilities decrease
654 from morning to noon for thin clouds and reach their daily minima at noon. In the afternoon, as a growing
655 percentage of thin clouds persist as thin clouds in previousduring the next hours, LWP and α_c susceptibilities
656 gradually increase to less negative and near zero, respectively. Table 1. Hypotheses for the diurnaldaytime variation
657 of LWP and CF susceptibilities for warm boundary layer clouds.

Hypotheses	Diurnal Daytime variation of LWP susceptibility			Daytime Diurnal variation of CF susceptibility	
	Non-precipitating thin clouds	Non-precipitating thick clouds	Precipitating clouds	Non-precipitating thin clouds	Non-precipitating thick clouds
H1. Changes in cloud morphology	N/A Not applicable.	Not applicable. N/A	Not applicable. N/A	Not applicable. N/A	Mostly overcast clouds in the morning and evening. CF of overcast clouds is less sensitive to perturbations.
H2. LWP responses to perturbations are slower than the state transition.	Non-precipitating thick clouds transition to thin clouds from morning to noon, which leads to a daily minimum LWP susceptibility	Thin clouds develop to thick clouds from noon to evening, which leads to an increase in LWP susceptibility.	Non-precipitating thin clouds transition to precipitating clouds in the afternoon, which leads to a decrease in LWP	Thick clouds transitioned to thin clouds from morning to noon, leading to a decrease in CF susceptibility	Cannot explain
H3. Dissipation or development of clouds	Cannot explain. Clouds that are growing or dissipating have similar LWP susceptibilities as clouds with constant CF.	Cannot explain.	Cannot explain.	Cannot explain.	Cannot explain.

659 660	Precipitating clouds	~~Not applicable.N/A~~	~~Thin clouds transition to precipitating clouds in the afternoon, and lead to a decrease in CF susceptibility.~~	~~Cannot explain~~

3.4.2 Non-precipitating thick clouds
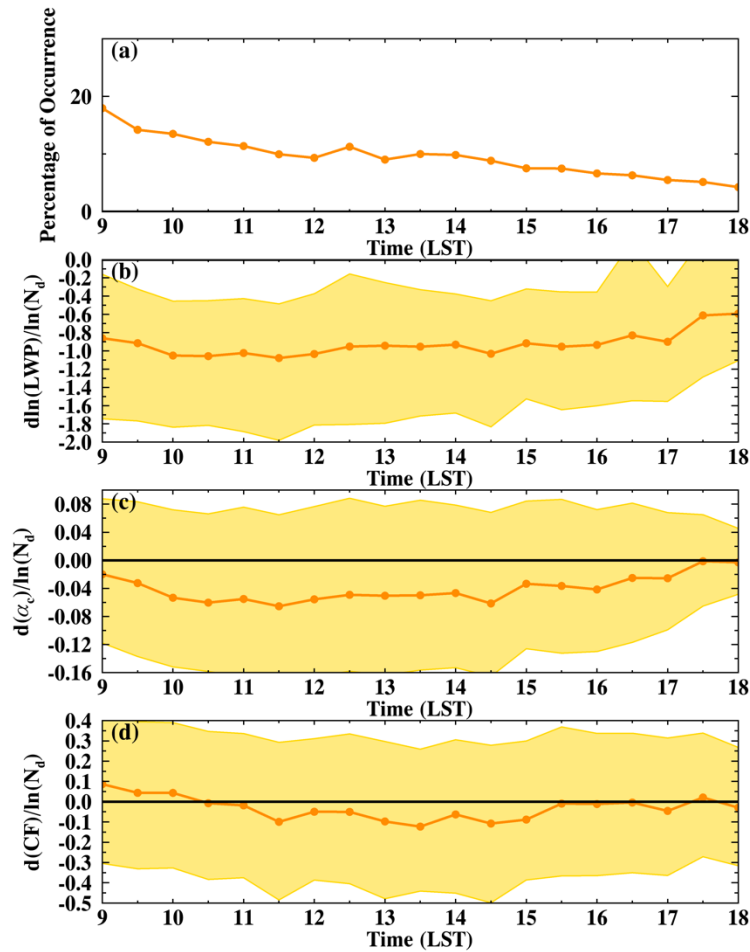
Figure 6. Daytime variation of (a) percentage of occurrence of non-precipitating thick clouds to warm boundary layer clouds, (b) cloud LWP susceptibility ($dln(LWP)/dln(N_d)$), (c) cloud albedo susceptibility ($d\alpha_c/dln(N_d)$), and (d) cloud fraction susceptibility ($dCF/dln(N_d)$) for non-precipitating thick clouds. The shaded areas represent the lower and upper 25th percentile of the cloud susceptibilities for each time step. and the solid lines with dots represent the mean valuesThe solid lines without symbols in (a)-(d) represent the daytime mean values.

Consistent with Fig. 2e, non-precipitating thick clouds are the least frequent warm boundary layer cloud state during summer over the ENA region. Their percentage of occurrence continuously decreases from 20% in the morning to less than 5% in the evening (Fig. 6a). As shown in Figs. 6b and c, theFor LWP and α_c, their susceptibilities for thick clouds first decrease from less negative to more negative in the morning and then increase from noon to evening (Fig. 6b and c, respectively). CF susceptibility is weakly positive in the early morning, becomes weakly negative from late morning to early afternoon, and increases to near zero in the evening (Fig. 6d). The diurnaldaytime variation evolutions of LWP and $\alpha_c$cloud susceptibilities for thick clouds exhibit consistent trend with is close to the cloud susceptibilities for thin clouds transition from thick clouds shown in Fig. 5 but with a lag of two hours. For example, the LWP susceptibility for thick clouds decreases from -0.8 to -1.1 from 9 to 11

26

678 LST and it increase from −1.1 to −0.8 from 11 to 16 LST; while the LWP susceptibility for the thick-to-thin

679 category in Fig. 5b decreases from −0.8 to −1.2 from 11-13 LST and increases to −0.6 from 13 to 18 LST. d (thick

680 → thin, dash line with diamond symbols), which This result supports our hypothesis on cloud retaining its memory

681 of AIE of its previous cloud state.

682 To gain insight into the observed evolution of LWP and α_c susceptibility from morning to evening, we

683 investigate the influence of cloud state transition on cloud susceptibility for non-precipitating thick clouds (Figure

684 7), which is summarized as H12 in Table 1. As shown in Fig. 7a, around 40% of thick clouds sustain as thick clouds

685 in from the previous two hours during in the morning period; whereases during the late afternoon to evening, with

686 decreasing solar radiation, more than 60% of thick clouds are developed from thin clouds in previous two hours.

687 Consistent with the findings presented in Fig. 5, thick clouds that are previously thick exhibit significantly more

688 negative LWP susceptibility compared to thick clouds that are previously thin (Fig. 7b). These differences are

689 particularly prominent in the from late morning to noon and become not insignificant in the afternoon. As discussed

690 before, difference between the thick-to-thick and the thin-to-thick categories are due to the LWP susceptibilities for

691 thick and thin clouds of previous time, while the smaller differences in the early morning and afternoon could be

692 attributed to the expected stronger turbulence and cloud coupling states at these times. . However, as the total

693 percentage of thick clouds decrease to less than 10% in the afternoon (Fig. 6a), the limited number of samples for all

694 three groups results in non-significant differences in LWP susceptibility among them. Additionally, Fig. 7d indicates

695 that transition in cloud state cannot account forexplain the diurnaldaytime variation in CF susceptibility for thick

696 clouds, as all three groups are insignificantly different from each other.
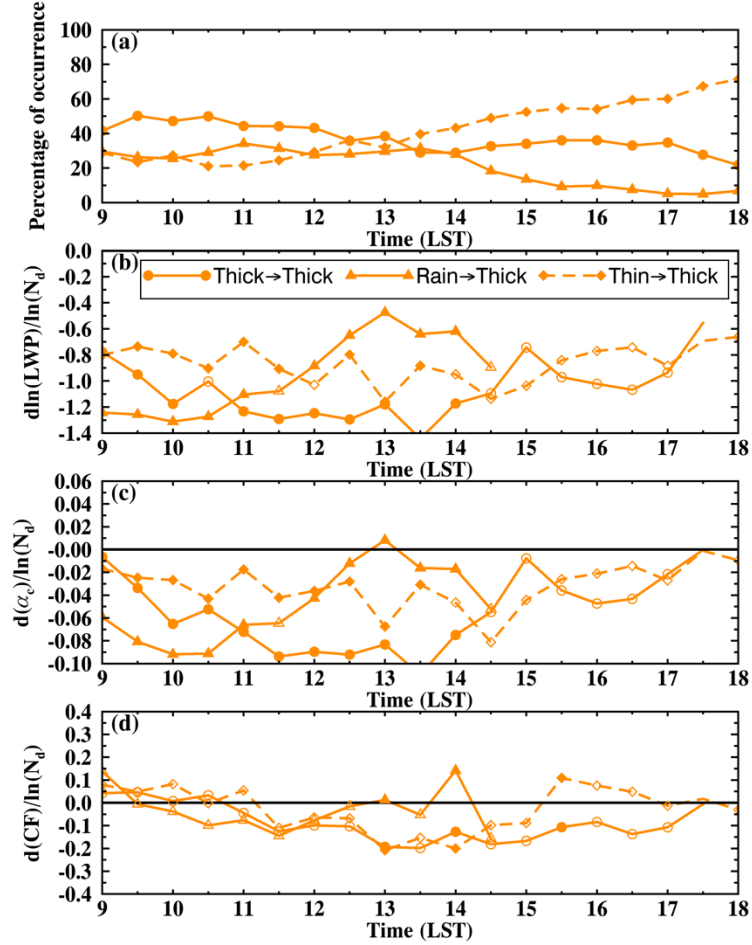
697
698 Figure 7. Daytime variation of non-precipitating thick clouds transition from non-precipitating thick clouds (thick →
699 thick, solid line with circle symbols), precipitating clouds (rain → thick, solid line with triangle symbols), and non-
700 precipitating thin clouds (thin → thick, dash line with diamond symbols) in previous two hours. Symbols for
701 different state transitions are noted in (b). In (b)-(d), filled markers indicate data points that are significantly
702 different from the other two groups (p<0.05), while open markers indicate statistical insignificance.

703   To understand the driving ~~force~~ mechanism for the ~~diurnal~~daytime variation in CF susceptibility shown in

704 Figure 6d, we calculate the mean cloud properties for non-precipitating thin and thick clouds, as shown in Fig.~~ure~~

705 ~~S38~~. In the morning, non-precipitating thick clouds are predominantly overcast clouds with a mean CF of 75% (Fig.

706 ~~S38~~a). To distinguish between overcast and broken clouds, we calculate the diameter-to-height ratio (DHR) for each

707 cloud, where diameter is estimated by the square root of the area and height is defined as the 90th percentile of cloud

708 tops. As shown in Fig. ~~S38~~c, thick clouds are mostly overcast in the morning with a mean DHR of 230. Compared to

709 broken clouds, overcast clouds have less room for CF to increase, which results in a less positive CF susceptibility

710 for thick clouds compare to thin ~~CF~~. After 10 am, non-precipitating thick clouds start to break. The mean CF

711 decreases from 75% at 10 am to 60% at 2 pm and the DHR decreases from 230 to 170. As CF for broken clouds is

712 more sensitive to N_d perturbations, CF susceptibility decreases to $-0.13 \, ln(N_d)^{-1}$, which is consistent with the

713 daytime mean negative CF susceptibility shown in Fig.2c. From afternoon to evening, clouds transition to overcast

714 again (Fig. ~~S38~~), and the CF susceptibility increases back to zero. This impact of cloud morphology (e.g., overcast

715 or broken clouds) on ~~diurnal~~daytime variation of CF susceptibility is summarized as H~~3~~1 in Table 1.
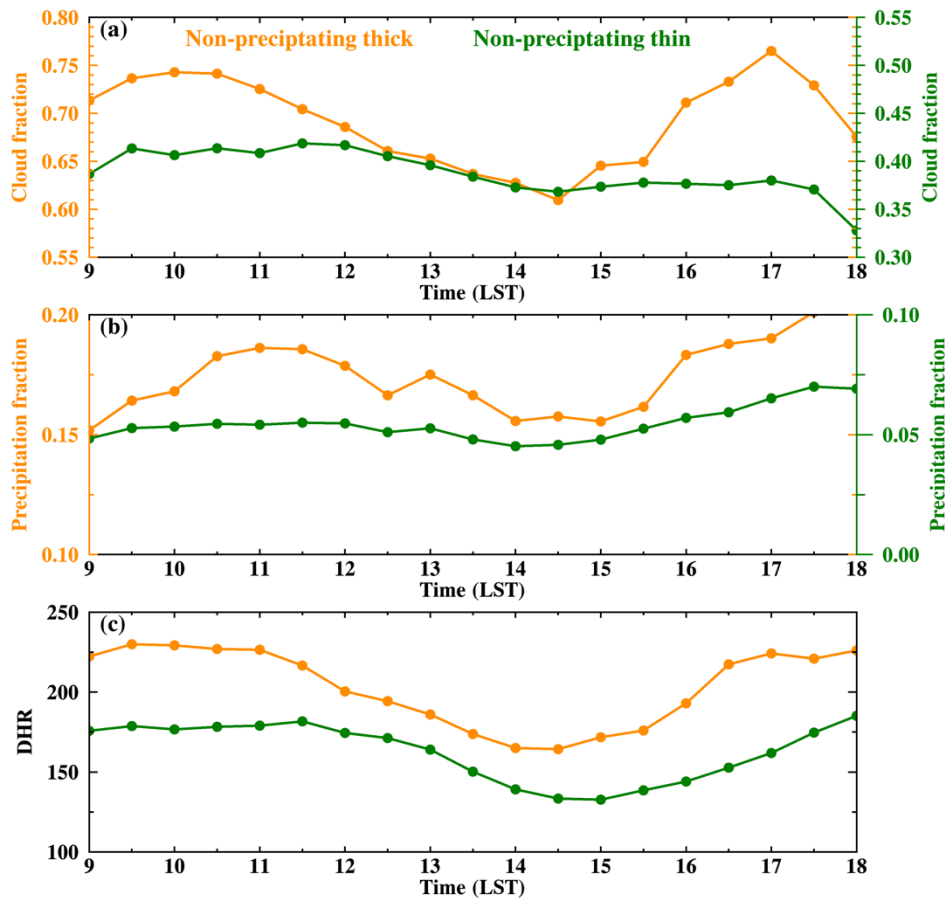
28

Figure 8. Diurnal variation of (a) cloud fraction, (b) pixel-level precipitation fraction, and (c) diameter-to-height ratio (DHR) for non-precipitating clouds. Different colors represent different cloud states as indicated in (a). Please note that the non-precipitating thin cloud in (a) and (b) use the y-axis on the right side.

In conclusionThe previous results are summarized as follows:, LWP susceptibility for non-precipitating thick clouds first decreases from less negative to more negative in the morning and then increase from noon to evening, which is likely attributed to the transition from thin to thick clouds. In the morning, 40% to 50% of thick clouds are previously thick clouds, these clouds exhibit a large negative LWP susceptibility. In the afternoon, 60-70% of with increasing percentage of thick clouds develop from thin clouds in previous hours and retain the memory of LWP susceptibility of thin cloud,s. Therefore, LWP susceptibility gradually increases in the afternoon, and becomes similar to that of thin clouds (Fig. 4b, 6b). DiurnalDaytime variation in CF susceptibility for thick clouds is likely attributed to changes in cloud morphology. In the morning and evening, thick clouds are mostly overcast with CF less sensitive to N_d perturbations, resulting in a near zero CF susceptibility. From late morning to early afternoon, the overcast thick clouds break down and CF decrease with increasing N_d likely due to the enhanced entrainment and evaporation.

The impact of cloud memory and transition of cloud state on the diurnaldaytime variation of LWP susceptibility is summarized as a schematic figure shown in Fig.ure 98. From morning to noon, as non-precipitating thick clouds transition to thin clouds, thin cloudsey retain their memory of the large negative LWP susceptibility of

29

734 their previous state. Therefore, LWP susceptibility for thin clouds decreases from morning to noon and reach its

735 daily minima in the early afternoon. From early afternoon to evening, with non-precipitating thin clouds developing

736 to thick clouds, LWP susceptibility for thick clouds increase.
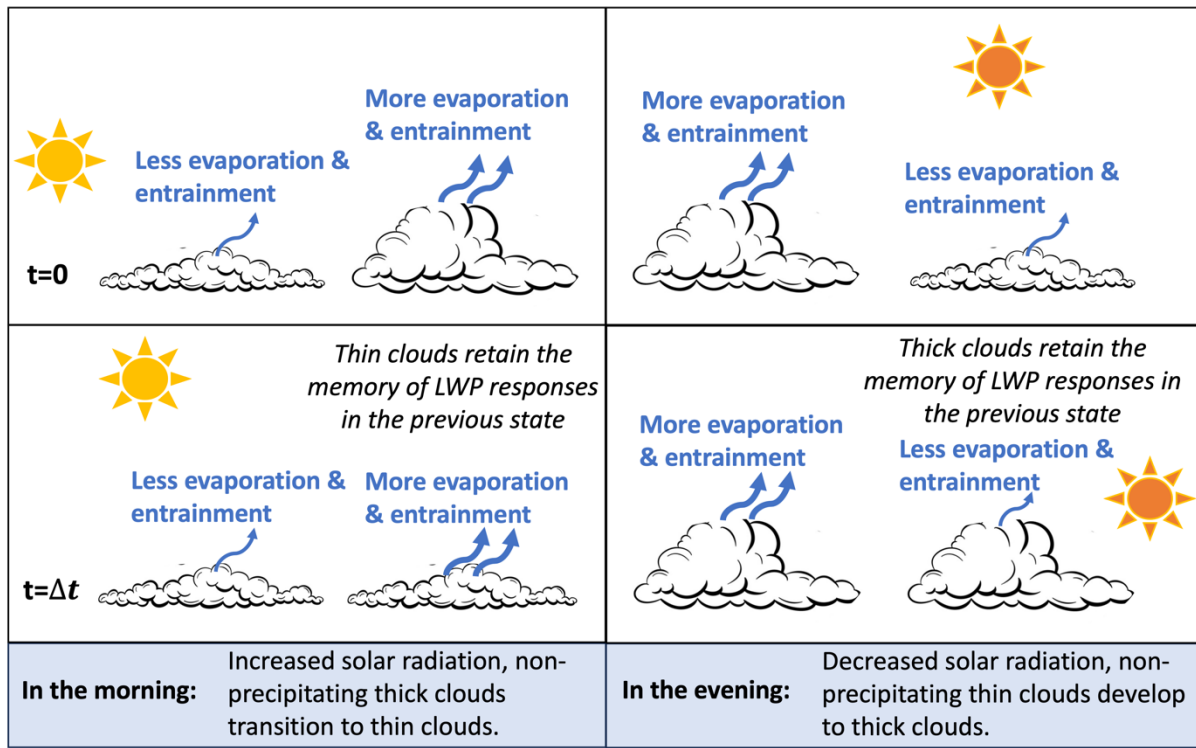
737
738 Figure 98. Schematic figure of influence of cloud memory and transition of cloud state on the LWP susceptibility
739 and its diurnaldaytime variation.

3.4.3 Precipitating clouds

741 PAs shown in Figure 9a, precipitating clouds, depicted in Figure 9Figs.10a, are the dominant cloud state in

742 this region, accounting for 46% of the warm boundary layer clouds, compared to 44% of non-precipitating thin

743 clouds. The frequency of precipitating clouds is higher in the morning and evening compared to noon. Throughout

744 the day, the mean LWP susceptibility remain consistently negative, fluctuating between -0.5 to -0.3, with

745 minimum values between 14–16 LST (Fig. 9Figs.10b). The diurnaldaytime variability in LWP susceptibility for

746 precipitating clouds is much lower than that for non-precipitating thin (e.g., from -0.9 to -0.4) and thick (e.g., from

747 -1.1 to -0.6) clouds. The negative LWP susceptibility is likely due to the prevalence of lightly precipitating clouds,

748 with a mean precipitating fraction ranging from 0.2 to 0.5 (Fig. S2d). The influence of precipitation suppression is

749 smaller than that of the entrainment enhancement. Similarly, α_c susceptibility fluctuates between 0 to 0.02

750 throughout the day, with near zero α_c susceptibility in early afternoon (Fig. 9Figs.10c). Despite the minimal

751 diurnaldaytime variation, the LWP and α_c susceptibilities at 13-16 LST are statistically significant different than

752 from cloud susceptibilities in the morning and evening at 95% confidence level with the two-tailed t-test. The CF

753 susceptibility for precipitating clouds also shows minimal diurnaldaytime variation compared to non-precipitating

754 clouds, with a mean value ranging from 0 to 0.1 (Fig. 9Figs.10d).

30
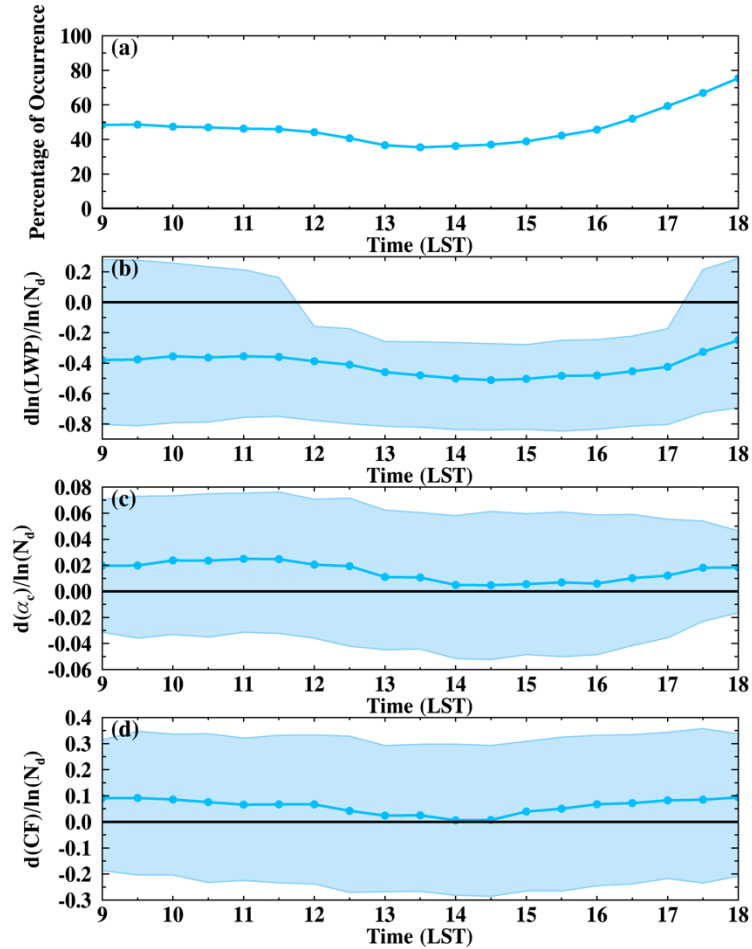
Figure 109. Daytime variation of (a) percentage of occurrence of precipitating clouds to warm boundary layer clouds, (b) cloud LWP susceptibility ($dln(LWP)/dln(N_d)$), (c) cloud albedo susceptibility ($d\alpha_c/dln(N_d)$), and (d) cloud fraction susceptibility ($dCF/dln(N_d)$) for precipitating clouds. The shaded areas represent the lower and upper 25th percentile of the cloud susceptibilities for each time step. ~~The solid lines without symbols in (a)-(d) represent the daytime mean values.~~

Consistent with non-precipitating clouds, the ~~diurnal~~daytime variation of LWP and α_c susceptibilities for precipitating clouds can be attributed to the transition of cloud states. For example, as shown in ~~Figure 10~~Figs.11b-d, precipitating clouds that transition from non-precipitating thin clouds exhibit significantly more negative/less positive cloud susceptibilities than precipitating clouds that are previously precipitating. Meanwhile, α_c and CF susceptibilities switch signs from positive to negative in the afternoon for precipitating clouds transition from non-precipitating thin clouds compared to that are previously precipitating (dash line with diamond symbols in Figs. 11c, d). Starting from 13 LST, when non-precipitating thin clouds transition to precipitating clouds (~~Fig. 10~~Fig.11a), LWP and α_c susceptibilities begin to decrease and reach their daily minimum in the late afternoon. Interestingly, as non-precipitating ~~thin~~ clouds transition to precipitating clouds (~~Fig. 10~~Figs.11b and c, thin → rain, thick → rain), their LWP and α_c susceptibilities exhibit both less negative values and smaller ~~diurnal~~daytime variations compared to thin/~~-~~thick clouds that remain as thin/thick (Figs. 5b and c, thin → thin, Figs. 7b and c, thick → thick). The underlying reason for this observation is currently unclear and ~~worth~~ warrants further investigation~~s~~ on the sensitivity of AIE for clouds experiencing transition in cloud states, especially between precipitating and non-

31

774 precipitating clouds. ~~Furthermore~~Lastly, the percentage of precipitating clouds that transition from non-precipitating

775 thick clouds is less than 7% (~~Fig. 10~~Fig.11a). ~~Due to the limited number of cases, precipitating clouds that evolve~~

776 ~~from non-precipitating thick clouds do not exhibit significantly more negative LWP susceptibilities, especially~~

777 ~~during the period from 11 to 14 LST when the transition percentage decreases to 3%.~~

778   In conclusion, precipitating clouds exhibit smaller ~~diurnal~~daytime variation in cloud susceptibilities

779 compared to non-precipitating thin and thick clouds. The decrease of LWP and α_c susceptibilities for precipitating

780 clouds in the afternoon is likely contributed by the transition of non-precipitating thin clouds to precipitating clouds.
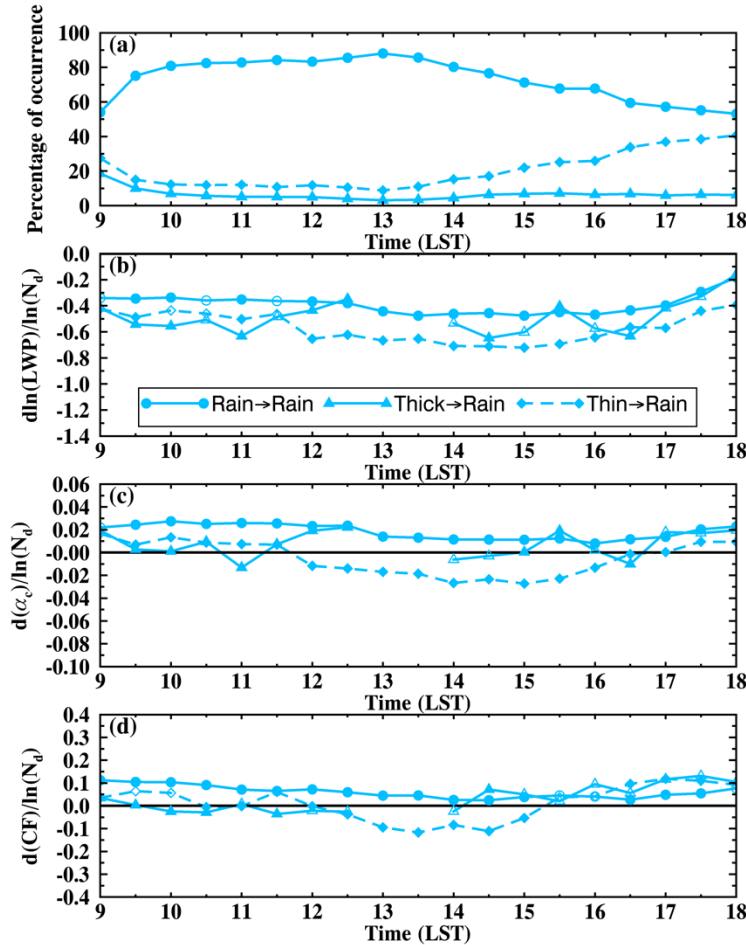
781
782 Figure 11~~0~~. Daytime variation of precipitating clouds transitioned from precipitating clouds (rain → rain, solid line
783 with circle symbols), non-precipitating thick clouds (thick → rain, solid line with triangle symbols), and non-
784 precipitating thin clouds (thin → rain, dash line with diamond symbols) in previous two hours. Symbols for different
785 state transitions are noted in (b). In (b)-(d), filled markers indicate data points that are significantly different from
786 the other two groups (p<0.05), while open markers indicate statistical insignificance.

787   Combining the results shown here and results in section 3.4.1, we can answer ~~the question raised at the end~~

788 ~~of~~in section 3.3~~:~~ which cloud state contributes the most to the daytime variation of cloud susceptibility. The non-

789 precipitating thin clouds exhibit similar ~~diurnal~~daytime variation_s in LWP, α_c, and CF susceptibility ~~as~~than the

790 warm boundary layer clouds~~-~~ (Fig.4 vs. Fig. 3), with clouds being less susceptible to N_d perturbations in the morning

791 and evening and more susceptible at noon. Additionally, non-precipitating thin clouds have highest frequency at

32

noon. On the other hand, precipitating clouds, despite their higher percentage of occurrence than thin clouds, exhibit minimal ~~diurnal~~daytime variation in cloud susceptibility. Therefore, the pronounced ~~diurnal~~daytime variations in cloud susceptibilities for warm boundary layer clouds primarily stem from non-precipitating thin clouds. The distinct daytime evolution patterns for the three clouds states highlight the importance of cloud state classification in quantification of cloud susceptibility. ~~In addition, the asymmetric evolution patterns of LWP, α_c, and CF susceptibility for non-precipitating thick and precipitating clouds indicate that the daytime variation of cloud susceptibility is not due to retrieval uncertainties related to SZA.~~

3.5 Contribution to the ~~diurnal~~daytime variation of cloud susceptibility

As discussed in the previous section, both the frequency of occurrence of cloud states and the intensity of cloud responses to N_d perturbations exhibit pronounced ~~diurnal~~daytime variations. In this section, we aim to compare the contribution of these two components to the overall ~~diurnal~~daytime variation in cloud susceptibilities by fixing one component constant at a time. The contribution from changes in the frequency of cloud states is represented by the red lines in ~~Fig.11~~Fig.12, which is estimated by weighting the daytime mean cloud susceptibility (Figs. 2a-c) with the half-hourly frequency of occurrence of clouds in the LWP-N_d parameter space, assuming a constant intensity of cloud susceptibility~~AIE~~ during the daytime. The contribution from changes in the intensity of cloud susceptibility~~AIE intensity~~ is depicted by the blue lines, which is estimated by weighting the half-hourly cloud susceptibility in the LWP-N_d parameter space with the daytime mean frequency of occurrence of clouds (Fig. 2e), assuming a constant frequency during the daytime. The black line in Fig. 12~~11~~ represents the observed susceptibility shown in Fig. 3, ~~which considers~~and it includes the contributions from ~~diurnal~~daytime variations in both components.
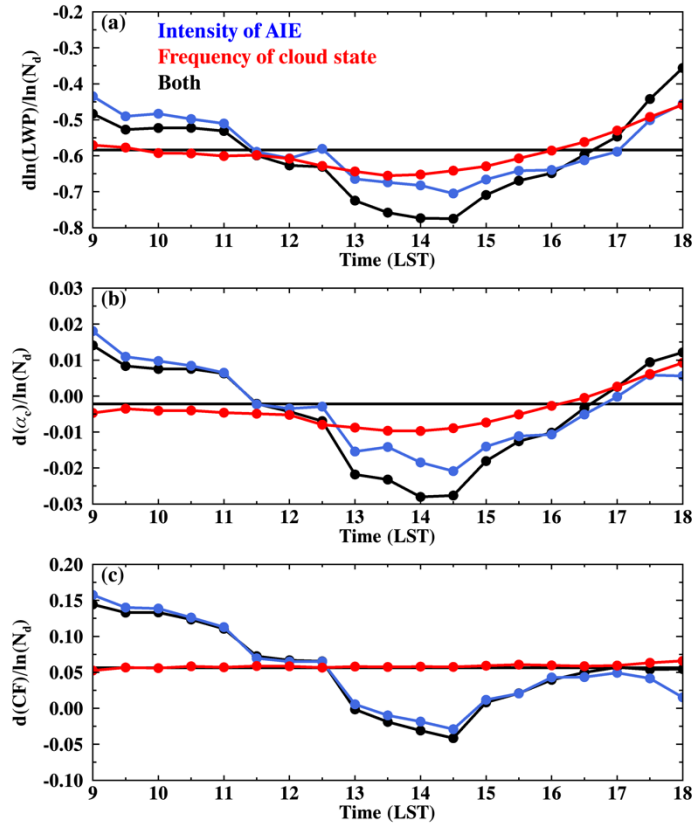
Figure 12̶1̶. Daytime variation in cloud susceptibility contributed from the variability in the intensity of susceptibility (blue lines with symbols), variability in the frequency of occurrence of cloud state (red lines with symbols), and from both (black lines with symbols). (a) cloud LWP susceptibility ($dln(LWP)/dln(N_d)$), (b) cloud albedo susceptibility ($d\alpha_c/dln(N_d)$), (c) cloud fraction susceptibility ($dCF/dln(N_d)$). The horizontal black solid lines w̶i̶t̶h̶o̶u̶t̶ ̶s̶y̶m̶b̶o̶l̶s̶ in (a)-(c) are the daytime mean susceptibility.

When comparing the net observed d̶i̶u̶r̶n̶a̶l̶daytime variation of cloud susceptibilities (black lines) with the contributions from changes in the intensity o̶f̶ ̶A̶I̶E̶ and the frequency of cloud state (blue and red lines, respectively), we find that the d̶i̶u̶r̶n̶a̶l̶daytime changes in cloud susceptibility is primarily driven by changes in the intensity of cloud susceptibilitiesA̶I̶E̶ during the day. Additionally, as shown in Figs. 12̶1̶1̶a and b, the red lines are close to the daytime mean values in the morning, which indicates that variations in the frequency of different cloud states have minimal impact on changes in LWP and α_c susceptibilities in the morning. On the other hand, in the afternoon, both shifts in cloud states and changes in intensities contribute to the changes in LWP and α_c susceptibilities. Compared with LWP and α_c susceptibilities, the daytime variation of CF susceptibility shows minimal sensitivity to changes in cloud state frequency. This limited impact stems from the fact that the daytime fluctuation in cloud state frequency is predominantly influenced by precipitating and non-precipitating thin clouds. Meanwhile, the daytime mean CF susceptibilities for precipitating and non-precipitating thin clouds closely align, measuring at 0.08 and 0.09, respectively (Fig. 2c). This convergence diminishes the influence of alterations in the frequency of these two cloud states.

In summary, the daytime variation of cloud susceptibility is largely driven by the variation in its intensity. S̶since polar-orbiting satellites c̶a̶n̶ only observe the i̶n̶t̶e̶n̶s̶i̶t̶y̶ ̶o̶f̶ ̶A̶I̶E̶cloud responses to N_d perturbations across

34

833 different cloud states at their overpass time, they cannot fully capture the diurnal variation of cloud susceptibilities

834 driven by the ~~diurnal~~ variation in ~~AIE intensity~~the intensity of cloud susceptibility. Given that all three cloud

835 susceptibilities reach their daily minimum at around 13:30 LST, studies based on polar-orbiting satellite with

836 overpass time at noon may ~~be~~ underestimat~~ing~~ the daily mean value of cloud susceptibility.

837 **4. Discussions**

838   In this study, we quantify the ~~instantaneous responses~~susceptibility of warm boundary layer clouds to N_d

839 perturbation using the pixel-level SEVIRI cloud retrievals of each time step. For heavily precipitating clouds, LWP

840 increases under pristine condition (e.g., $N_d < 30\ cm^{-3}$, Fig. 2a). For lightly precipitating and non-precipitating

841 clouds, LWP decreases with N_d. The N_d-LWP relationship found ~~fouind~~ in this study is consistent with that in

842 Gryspeerdt et al. (2019) using global mean cloud retrievals from MODIS and AMSR-E at coarser resolution of

843 $1° \times 1°$ and daily timescale. This consistency between different satellite measurements at different temporal and

844 spatial scales greatly enhance our confidence in the retrieved relationship.

845   This study further distinguishes non-precipitating clouds into thin and thick clouds based on their LWP. A

846 consistent decreasing trend in cloud water is found for both states, yet non-precipitating thick clouds exhibit more

847 negative LWP susceptibility ($\frac{dln(LWP)}{dln(N_d)} = -0.94$) compared to thin clouds ($\frac{dln(LWP)}{dln(N_d)} = -0.71$). The LWP

848 susceptibilities estimated in this study are more negative than those in Zhang et al. (2022) and Zhang and Feingold

849 (2023), based on similar classification of cloud states. Particularly, we found that non-precipitating thin clouds have

850 a decreasing trend in cloud water and a warming effect at~~on~~ the surface radiation while these are opposite in Zhang

851 et al. (2022) and Zhang and Feingold (2023). ~~We speculate this difference~~ This is due to different seasons and study

852 regions between our and their studies. The summer boundary layer in the ENA region is deeper and less stable with

853 higher cloud tops ~~is due to the less stable troposphere, deeper boundary layer, and the higher cloud tops over the~~

854 ~~ENA regions~~ (e.g., Klein and Hartmann, 1993; Ding et al., 2021; King et al., 2013) compared to the NE Pacific in

855 Zhang et al. (2022) and the ~~study regions~~NE Atlantic region in Zhang and Feingold (2023). The less stable

856 condition~~.~~, ~~over the studied region leads to a~~ deeper boundary layer, and deeper clouds could ~~lead to and~~ a stronger

857 cloud-top entrainment rate ~~at the cloud top, all of which may cause~~ and result in a more negative LWP susceptibility

858 (Possner et al., 2020; Toll et al., 2019).

859   Regarding the CF adjustment to N_d perturbation, a daytime mean positive response is found for

860 precipitating and non-precipitating thin clouds and a negative response for non-precipitating thick clouds (Fig. 2c).

861 Few studies have quantified the ~~instantaneous~~ CF adjustment rate at 30-minute intervals ~~at 30-mins resolution~~ for a

862 direct~~ly~~ comparison of CF susceptibility. However, similar results are found using measurements and retrievals from

863 different platforms at various spatial and timescales, which greatly increase our confidence in the observed CF

864 responses toward N_d perturbation. For example, using MODIS measurement, Kaufman et al. (2005) found an

865 increase in the longitudinal mean cloudiness for warm boundary layer clouds with increasing AOD in all four

866 regions of the Atlantic Ocean characterized by distinct aerosol types. Using the natural experiment of volcanic

867 eruption at Holuhraun in Iceland, Chen et al. (2022) found that aerosols from the eruption increase the monthly

868 mean cloud cover by 10% over the North Atlantic. By tracking the cloud trajectory using geostationary satellites,

869 Christensen et al. (2020) found that aerosol enhance both CF and cloud lifetime in the timescale of 2-3 days,

870 especially under stable conditions. It is worth noting that a decrease in CF was not observed in these studies, likely

871 due to the prevalence of non-precipitating thin clouds and precipitating clouds in the Atlantic or the NE Pacific (e.g.,

872 Zhang and Feingold, 2023) that mask the signal from non-precipitating thick clouds without distinguishing cloud

873 states.

874 Lastly, the distinct "U-shaped" daytime variation in all three cloud properties found in this study (Fig. 3a-c)

875 is *unlikely* due to the systematic bias in r_e and τ retrievals at large SZA based on the following two aspects. Firstly,

876 if the daytime variation is driven by retrieval bias at large SZA, we would expect the susceptibility exhibiting a

877 symmetric pattern at local noon. As shown in Figs. 10 and 6, the LWP and α_c susceptibilities for precipitating and

878 non-precipitating thick clouds exhibit asymmetric pattern at local noon: with a decreasing trend from 13 LST and a

879 daily minimum at 16 LST, and a continuously increasing trend from 11 to 18 LST, respectively. In addition, the CF

880 susceptibilities for all three cloud states show asymmetric patterns at local noon. Secondly, if the retrieval

881 uncertainty dominates the signal, we would expect less variation in cloud susceptibilities for overcast clouds, which

882 suffer less uncertainties in cloud retrievals from the plane-parallel assumption and the cloud 3-D effect. However,

883 the opposite is found from the sensitivity test where overcast clouds exhibit stronger daytime variation in cloud

884 susceptibilities (not shown).

885 **5. Conclusions**

886 Using N_d as an intermediary variable, this study investigates the aerosol indirect effect (AIE) for warm boundary

887 layer clouds and its ~~diurnal~~daytime variation over the ENA region with the half-hourly and 3-km cloud property

888 retrievals from SEVIRI on the Meteosat-11. To constrain meteorological impacts on clouds and aerosol-cloud

889 interaction, cloud susceptibilities are estimated within a 1° × 1° grid box for each satellite time step. Based on the

890 daytime mean cloud susceptibilities in the LWP-N_d parameter space, the sign and magnitude of cloud

891 susceptibilities strongly depend on the cloud states (Fig. 2). Accordingly, warm boundary layer clouds are classified

892 into three states: precipitating clouds (r_e>15 μm), non-precipitating thick clouds (r_e<15 μm, LWP > 75 gm^{-2}), and

893 non-precipitating thin clouds (r_e<15 μm, LWP < 75 gm^{-2}).

894

895 Precipitating clouds exhibit contrasting responses in cloud LWP, with increases observed for heavily

896 precipitating clouds and decreases for lightly precipitating clouds. Positive α_c and CF susceptibilities are identified

897 for both heavily and lightly precipitating clouds. The net all-sky radiative forcing of the AIE on precipitating clouds

898 is estimated to be $-13\ W\ m^{-2}ln(N_d)^{-1}$, with contributions from the CF and α_c effects of −9.5 and −3.5

899 $W\ m^{-2}\ ln(N_d)^{-1}$, respectively.

900 For non-precipitating clouds, both thick and thin clouds show negative LWP susceptibility with more

901 negative values found for thick clouds with higher LWP and N_d. This is likely attributed to the larger cloud top

902 radiative cooling rate and stronger entrainment for thick clouds. ~~becomes more negative with increasing LWP and~~ ,

36

~~likely due to the enhanced entrainment, leading to stronger evaporation and reductions in LWP with increased .~~

Consistent with the evaporation-entrainment feedback ~~hypothesis,~~, non-precipitating thick clouds exhibit ~~decreasing~~ a decrease in CF and α_c with increasing N_d, and ~~have~~ results in a net warming effect at the surface and a radiative forcing of +4.4 $W\ m^{-2}\ ln(N_d)^{-1}$. On the other hand, non-precipitating thin clouds show an increasing response in CF and a ~~weaker LWP and~~ responses and ~~less~~ negative α_c susceptibility ~~an increasing response in CF~~. Additionally, the radiative effect from increasing CF ($-8.3\ W\ m^{-2}\ ln(N_d)^{-1}$) outweighs that from a darker cloud ($+3.1\ W\ m^{-2} ln(N_d)^{-1}$) and ~~The increase in CF compensates for the decrease of and~~ leads to a net cooling effect of -5.2~~4.3~~ $W\ m^{-2}\ ln(N_d)^{-1}$.

Warm boundary layer clouds ~~exhibit strong~~manifest distinct and significant (p<0.05) ~~diurnal~~daytime variations in ~~cloud~~ LWP, α_c, and CF susceptibilities~~.,~~ with ~~all~~All three cloud susceptibilities exhibi~~ting~~ "U-shaped" diurnal patterns with clouds being less susceptible in the morning and evening and more susceptible at local noon ~~where susceptibilities are lowest during the early afternoon~~ (Fig. 3). ~~Meanwhile, there is little spatial variability in cloud susceptibilities in the study region and the diurnal cycle of cloud susceptibility over the 1° × 1° box at the ARM ENA site agree well with the domain mean value, which imply the regional representativeness of the ARM ENA site of AIE.~~ Based on our analysis of the ~~diurnal~~daytime variation of cloud susceptibility for different cloud ~~states (Figs. 4, 6, 9), we find that the diurnal~~daytime variations in cloud susceptibilities for all warm boundary layer ~~clouds are primarily driven by non-precipitating thin clouds. They have similar "U-shaped" diurnal~~daytime patterns ~~in cloud susceptibilities and constitute approximately 44% of the warm boundary layer clouds in this region (Fig. 4).~~

~~Diurnal~~Daytime variation in LWP and α_c susceptibilities ~~for non-precipitating thin clouds~~ is likely ~~due~~ attributed to the ~~combined effect of~~ transition in cloud state while clouds sustaining the memory of responses to N_d of the previous state~~and the relatively slow cloud~~ower response of clouds to ~~perturbation than the satellite~~at ~~timescales greater than 30 min~~ (H1~~2~~ in Table 1). From morning to noon, with increasing solar radiation, non-precipitating thick clouds evolve to thin clouds. Thin clouds decayed from thick show significantly more negative LWP and α_c susceptibilities than thin clouds that are previously thin (Fig. 5). Therefore, LWP and α_c susceptibilities decrease from morning to noon for thin clouds and reach their daily minima at noon (Fig.4). In the afternoon, thin clouds develop to thick clouds while retaining the memory of less susceptible to N_d perturbations (Fig. 7) and therefore leads to an increase in LWP and α_c susceptibilities for nonprecipitating thick clouds in the afternoon (Fig.6). ~~As non-precipitating clouds transition from thick to thin, the "memory" of LWP responses to perturbations is retained. Consequently, the LWP susceptibility for thin clouds transition from thick clouds is 0.2-0.4 more negative compared to those that are previously thin clouds, which accounts for 40-60% of the observed changes (Fig. 5). The differences are larger in the morning when cloud state transitions are more frequent. Similarly, non-precipitating thick clouds that develop from thin clouds in previous hours exhibit 0.2-0.5 less negative LWP susceptibility than thick clouds that remain consistently thick (Fig. 7).~~ Meanwhile, ~~diurnal~~daytime variation in CF susceptibility for non-precipitating thick clouds is more likely driven by changes in cloud morphology rather than the transition of cloud state (Fig. ~~S3~~8, ~~H1~~H3 in Table 1). Compared to non-precipitating clouds, precipitating clouds exhibit smaller ~~diurnal~~daytime variation in cloud susceptibility (~~Fig. 9~~Figs.10). ~~The decrease of cloud susceptibility~~

940 ~~for precipitating clouds in the afternoon is likely attributed to the transition of non-precipitating thin clouds to~~
941 ~~precipitating clouds. (Fig. 10).~~
942 The ~~diurnal~~daytime variation in cloud susceptibility is primarily driven by changes in the intensity of cloud
943 susceptibilities~~AIE~~ from morning to noon, rather than changes in the frequency of occurrence of different cloud
944 states (Fig. 12~~11~~). As the polar-orbiting satellites only observe cloud susceptibilities across different cloud states
945 during a specific overpass time, they overlook the change in the intensity of cloud susceptibilities during the day.
946 ~~and all three cloud susceptibilities reach their daily minimum at noon. Based on the estimated diurnal~~daytime
947 ~~variation, using~~More specifically, based on the daytime variation of cloud susceptibilities found in this study,
948 ~~satellite retrievals~~LWP susceptibility estimated at 13:30 LST could underestimate the daytime mean value ~~of LWP~~
949 ~~susceptibility~~ by 26.3% (-0.76 compared to -0.60), underestimate the α_c susceptibility by 475% (-0.023
950 compared to -0.004), and underestimate the CF susceptibility by 120% (-0.019 compared to $+0.055$). ~~Noticee~~ It is
951 worth noting that both the daytime variation and the daytime mean values of cloud susceptibilities in this study are
952 estimated based on the regression analysis on spatial data within each satellite time step, with the assumption that
953 the temporal change of cloud properties from N_d perturbations can be represented by the spatial relationships.
954 This study underscores the importance of considering the diurnal cycle of cloud susceptibilities when
955 quantifying AIE and their impacts on clouds and radiation. The classification of cloud states enables us to
956 distinguish the sign, magnitude, and underlying processes driving the diurnal variation of AIE.
957 To further advance our understanding of the diurnal variation of AIE, several avenues for future research
958 can be pursued. Firstly, it is important to address uncertainties associated with satellite retrievals, which can
959 propagate into uncertainties in the retrieved N_d, as discussed in Grosvenor et al. (2018). Future study could utilize
960 active sensors to reduce these uncertainties, particularly during nighttime conditions. Moreover, using the retrieved
961 N_d as a proxy of aerosol concentration may introduce uncertainties related to cloud processes that can act as sources
962 or sinks of N_d, potentially buffer the relationships between N_d and cloud condensation nuclei. Future investigations
963 are needed to better understand the relationships, and how they vary with different cloud processes and throughout
964 the day. Lastly, this study encompasses all warm boundary layer clouds without considering the highly diverse
965 meteorological regimes and the associated cloud types in the ENA region. Classification of the synoptic and
966 meteorological conditions associated with different cloud states and aerosol properties would contribute to a more
967 comprehensive understanding, allowing for the disentanglement of the impacts of meteorology from AIE.
968
969

970 **Data availability:**

971 SEVIRI Meteosat-11 cloud retrieval products, produced by NASA LaRC SatCORPS group, are available from the
972 Atmospheric Radiation Measurement (ARM) Data Discovery website at https://adc.arm.gov/discovery/, Minnis
973 Cloud Products Using Visst Algorithm (visstgridm11minnis). The ARM ground-based radar and lidar observations
974 are available from ARM Data Discovery, KAZRARSCL, (arsclkazr1kollias).
975

990 **Competing interests:**

991 The authors declare that they have no conflict of interest.

992

993

References

Albrecht, B. A.: Aerosols, Cloud Microphysics, and Fractional Cloudiness, Science, 245, 1227–1230,
https://doi.org/10.1126/science.245.4923.1227, 1989.

Arola, A., Lipponen, A., Kolmonen, P., Virtanen, T. H., Bellouin, N., Grosvenor, D. P., Gryspeerdt, E., Quaas, J., &
Kokkola, H. (2022). Aerosol effects on clouds are concealed by natural cloud heterogeneity and satellite
retrieval errors. Nature Communica)ons, 13(1), 7357. hrps://doi.org/10.1038/s41467-022-34948-5

Bennartz, R.: Global assessment of marine boundary layer cloud droplet number concentration from satellite, J.
Geophys. Res.,112, D02201, doi:10.1029/2006JD007547, 2007.

Bennartz, R. and Rausch, J.: Global and regional estimates of warm cloud droplet number concentration based on 13
years of AQUA-MODIS observations, Atmos. Chem. Phys., 17, 9815–9836, https://doi.org/10.5194/acp-17-
9815-2017, 2017.

Bréon, F.-M., Tanré, D., and Generoso, S.: Aerosol effect on cloud droplet size monitored from satellite, Science,
295, 834–838, 2002.

Bretherton, C. S., Blossey, P. N., and Uchida, J.: Cloud droplet sedimentation, entrainment efficiency, and
subtropical stratocumulus albedo, Geophys. Res. Lett., 34, L03813, https://doi.org/10.1029/2006GL027648,
2007.

Brenguier, J. L., Burnet, F., & Geoffroy, O.: Cloud optical thickness and liquid water path – does the coefficient
vary with droplet concentration? *Atmospheric Chemistry and Physics*, *11*(18), 9771-9786.
https://doi.org/10.5194/acp-11-9771-2011, 2011

Chen, Y.-C., Christensen, M., Stephens, G. L., and Seinfeld, J. H.: Satellite-based estimate of global aerosol–cloud
radiative forcing by marine warm clouds, Nature Geosci., 7, 643–646, https://doi.org/10.1038/ngeo2214, 2014.

Chen, Y., Haywood, J., Wang, Y., Malavelle, F., Jordan, G., Partridge, D., Fieldsend, J., De Leeuw, J., Schmidt, A.,
Cho, N., Oreopoulos, L., Platnick, S., Grosvenor, D., Field, P., & Lohmann, U.: Machine learning reveals
climate forcing from aerosols is dominated by increased cloud cover. *Nature Geoscience*, *15*(8), 609-614, 2022.
https://doi.org/10.1038/s41561-022-00991-6

Christensen, M. W., Jones, W. K., and Stier, P.: Aerosols enhance cloud lifetime and brightness along the stratus-
tocumulus transition, P. Natl. Acad. Sci. USA, 117, 17591–17598, https://doi.org/10.1073/pnas.1921231117,
2020.

Comstock, K. K., Wood, R., Yuter, S. E., and Bretherton, C. S.: Reflectivity and rain rate in and below drizzling
stratocumulus, Q. J. Roy. Meteorol. Soc., 130, 2891–2918, doi:10.1256/qj.03.187, 2004.

Ding, F., Iredell, L., Theobald, M., Wei, J., & Meyer, D. :. PBL Height From AIRS, GPS RO, and MERRA-2
Products in NASA GES DISC and Their 10-Year Seasonal Mean Intercomparison. *Earth and Space Science*,
8(9). https://doi.org/10.1029/2021ea001859, 2021

Dong, X., Xi, B., Kennedy, A., Minnis, P., & Wood, R.: A 19-month record of marine aerosol–cloud–radiation
properties derived from DOE ARM mobile facility deployment at the Azores. Part I: Cloud fraction and single-
layered MBL cloud properties. Journal of Climate, 27(10), 3665–3682. https://doi.org/10.1175/JCLI-D-13-
00553.1, 2014.

40

Dong, X., Xi, B., Qiu, S., Minnis, P., Sun-Mack, S., & Rose, F. : A radiation closure study of Arctic stratus cloud microphysical properties using the collocated satellite-surface data and Fu-Liou radiative transfer model. *Journal of Geophysical Research: Atmospheres*, *121*(17), 10,175-110,198. https://doi.org/10.1002/2016jd025255, 2016

Dong, X., Zheng, X., Xi, B., & Xie, S.: A Climatology of Midlatitude Maritime Cloud Fraction and Radiative Effect Derived from the ARM ENA Ground-Based Observations. Journal of Climate, 36(2), 531–546, https://doi.org/10.1175/JCLI-D-22-0290.1, 2023.

Duong, H. T., Sorooshian, A., and Feingold, G.: Investigating potential biases in observed and modeled metrics of aerosol-cloud precipitation interactions, Atmos. Chem. Phys., 11, 4027–4037, doi:10.5194/acp-11-4027-2011, 2011.

Fan, J. W., Wang, Y., Rosenfeld, D., and Liu, X. H.: Review of aerosol-cloud interactions: mechanisms, significance, and challenges, J. Atmos. Sci., 73, 4221–4252, 2016.

Feingold G, Eberhard W, Veron D, Previdi M. First measurements of the Twomey indirect effect using ground-based remote sensors. Geophys Res Lett. 30 (6). https://doi.org/10.1029/2002GL016633, 2003.

Feingold, G., Goren, T., & Yamaguchi, T. (2022). Quantifying albedo susceptibility biases in shallow clouds. Atmospheric Chemistry and Physics, 22(5), 3303–3319. https://doi.org/10.5194/acp-22-3303-2022.

Glassmeier, F., Hoffmann, F., Johnson, J. S., Yamaguchi, T., Carslaw, K. S., and Feingold, G.: Aerosol-cloud-climate cooling overestimated by ship-track data, Science, 371, 485–489, https://doi.org/10.1126/science.abd3980, 2021.

Grosvenor, D. P., & Wood, R.: The effect of solar zenith angle on MODIS cloud optical and microphysical retrievals within marine liquid water clouds. *Atmospheric Chemistry and Physics*, *14*(14), 7291-7321. https://doi.org/10.5194/acp-14-7291-2014, 2014

Grosvenor, D. P., Sourdeval, O., Zuidema, P., Ackerman, A., Alexandrov, M. D., Bennartz, R., Boers, R., Cairns, B., Chiu, J. C., Christensen, M., Deneke, H., Diamond, M., Feingold, G., Fridlind, A., HÃOEnerbein, A., Knist, C., Kollias, P., Marshak, A., McCoy, D., Merk, D., Painemal, D., Rausch, J., Rosenfeld, D., Russchenberg, H., Seifert, P., Sinclair, K., Stier, P., van Diedenhoven, B., Wendisch, M., Werner, F., Wood, R., Zhang, Z., and Quaas, J.: Remote Sensing of Droplet Number Concentration in Warm Clouds: A Review of the Current State of Knowledge and Perspectives, Rev. Geophys., 56, 409–453, https://doi.org/10.1029/2017RG000593, 2018.

Gryspeerdt, E., Quaas, J., and Bellouin, N.: Constraining the aerosol influence on cloud fraction, J. Geophys. Res.-Atmos., 121, 3566– 3583, https://doi.org/10.1002/2015JD023744, 2016.

Gryspeerdt, E., Goren, T., Sourdeval, O., Quaas, J., Mülmenst.dt, J., Dipu, S., Unglaub, C., Gettelman, A., and Christensen, M.: Constraining the aerosol influence on cloud liquid water path, Atmos. Chem. Phys., 19, 5331–5347, https://doi.org/10.5194/acp-19-5331-2019, 2019.

Gryspeerdt, E., Goren, T., and Smith, T. W. P.: Observing the timescales of aerosol–cloud interactions in snapshot satellite images, Atmos. Chem. Phys., 21, 6093–6109, https://doi.org/10.5194/acp-21-6093-2021, 2021.

Gryspeerdt, E., McCoy, D. T., Crosbie, E., Moore, R. H., Nott, G. J., Painemal, D., Small-Griswold, J., Sorooshian, A., and Ziemba, L.: The impact of sampling strategy on the cloud droplet number concentration estimated from satellite data, Atmos.Meas. Tech., 15, 3875–3892, https://doi.org/10.5194/amt-15-3875-2022, 2022.

Han, Q., Rossow, W. B., Zeng, J., and Welch, R.: Three Different Behaviors of Liquid Water Path of Water Clouds in Aerosol–Cloud Interactions, J. Atmos. Sci., 59, 726–735, https://doi.org/10.1175/1520-0469(2002)059<0726:TDBOLW>2.0.CO;2, 2002.

Kaufman, Y. J., Koren, I., Remer, L. A., Rosenfeld, D., & Rudich, Y.: The effect of smoke, dust, and pollution aerosol on shallow cloud development over the Atlantic Ocean. *Proc Natl Acad Sci U S A*, *102*(32), 11207-11212. https://doi.org/10.1073/pnas.0505191102, 2005

King, M. D., Platnick, S., Menzel, W. P., Ackerman, S. A., & Hubanks, P. A.: Spatial and Temporal Distribution of Clouds Observed by MODIS Onboard the Terra and Aqua Satellites. *IEEE Transactions on Geoscience and Remote Sensing*, *51*(7), 3826-3852. https://doi.org/10.1109/tgrs.2012.2227333, 2013

Klein, S. A., & Hartmann, D. L.: The seasonal cycle of low stratiform clouds. Journal of Climate, 6(8), 1587–1606. https://doi.org/10.1175/1520-0442(1993)006<1587:tscols>2.0.co;2, 1993.

Liu, J., Li, Z., and Cribb, M.: Response of marine boundary layer cloud properties to aerosol perturbations associated with meteorological conditions from the 19-month AMF-Azores campaign, J. Atmos. Sci., 73, 4253–4268, https://doi.org/10.1175/JAS-D- 15-0364.1, 2016.

Mather, J. H., & Voyles, J. W.: The Arm Climate Research Facility: A Review of Structure and Capabilities, *Bull. Am. Meteorol. Soc.*, 94, 377-392, https://doi.org/10.1175/BAMS-D-11- 00218.1, 2013.

Mechem, D. B., Wittman, C. S., Miller, M. A., Yuter, S. E., and De Szoeke, S. P.: Joint synoptic and cloud variability over the Northeast Atlantic near the Azores, J. Appl. Meteorol. Clim., 57, 1273–1290, 2018.

Minnis, P., Sun-Mack, S., Young, D. F., Heck, P. W., Garber, D. P., Chen, Y., Spangenberg, D. A., Arduini, R. F., Trepte, Q. Z., Smith, W. L., Ayers, J. K., Gibson, S. C., Miller, W. F., Hong, G., Chakrapani, V., Takano, Y., Liou, K., Xie, Y., and Yang, P.: CERES edition-2 cloud property retrievals using TRMM VIRS and Terra and Aqua MODIS data–Part I: Algorithms, IEEE Trans. Geosci. Remote Sens., 49, 4374–4400, https://doi.org/10.1109/TGRS.2011.2144601, 2011.

Minnis, P., K. Bedka, Q. Trepte, C. R. Yost, S. T. Bedka, B. Scarino, K. Khlopenkov, and M. M. Khaiyer: A consistent long-term cloud and clear-sky radiation property dataset from the Advanced Very High Resolution Radiometer (AVHRR). Climate Algorithm Theoretical Basis Document (C-ATBD), CDRP-ATBD-0826 Rev 1 - NASA, NOAA CDR Program, 159 pp., DOI:10.789/V5HT2M8T, https://www1.ncdc.noaa.gov/pub/data/sds/cdr/CDRs/AVHRR_Cloud_Properties_NASA/AlgorithmDescription _01B-30b.pdf, 2016.

Minnis, P., Sun-Mack, S., Chen, Y., Chang, F., Yost, C. R., Smith, W. L., Heck, P. W., Arduini, R. F., Bedka, S. T., Yi, Y., Hong, G., Jin, Z., Painemal, D., Palikonda, R., Scarino, B. R., Spangenberg, D. A., Smith, R. A., Trepte, Q. Z., Yang, P., and Xie, Y.: CERES MODIS Cloud Product Retrievals for Edition 4–Part I: Algorithm Changes, IEEE T. Geosci. Remote, 11152, 1–37, https://doi.org/10.1117/12.2532931, 2020.

Morrison, H., van Lier-Walqui, M., Fridlind, A. M., Grabowski, W. W., Harrington, J. Y., Hoose, C., et al.:
    Confronting the challenge of modeling cloud and precipitation microphysics. Journal of Advances in Modeling
    Earth Systems, 12, e2019MS001689. https://doi.org/10.1029/2019MS001689, 2020.

Painemal, D., Minnis, P., and Sun-Mack, S.: The impact of horizontal heterogeneities, cloud fraction, and liquid
    water path on warm cloud effective radii from CERES-like Aqua MODIS retrievals, Atmos. Chem. Phys., 13,
    9997–10003, https://doi.org/10.5194/acp-13-9997-2013, 2013.

Painemal, D.: Global Estimates of Changes in Shortwave Low-Cloud Albedo and Fluxes Due to Variations in Cloud
    Droplet Number Concentration Derived From CERES-MODIS Satellite Sensors, Geophys. Res. Lett., 45,
    9288–9296, https://doi.org/10.1029/2018GL078880, 2018.

Painemal, D., Spangenberg, D., Smith Jr.,W. L., Minnis, P., Cairns, B., Moore, R. H., Crosbie, E., Robinson, C.,
    Thornhill, K. L., Winstead, E. L., and Ziemba, L.: Evaluation of satellite retrievals of liquid clouds from the
    GOES-13 imager and MODIS over the midlatitude North Atlantic during the NAAMES campaign, Atmos.
    Meas. Tech., 14, 6633–6646, https://doi.org/10.5194/amt-14-6633-2021, 2021.

Penner, J. E., Dong, X., and Chen, Y.: Observational evidence of a change in radiative forcing due to the indirect
    aerosol effect, Nature, 427, 231–234, 2004.

Possner, A., Eastman, R., Bender, F., & Glassmeier, F.: Deconvolution of boundary layer depth and aerosol
    constraints on cloud water path in subtropical stratocumulus decks. *Atmospheric Chemistry and Physics*, *20*(6),
    3609-3621. https://doi.org/10.5194/acp-20-3609-2020, 2020

Rémillard, J., Kollias, P., Luke, E., and Wood, R.: Marine Boundary Layer Cloud Observations in the Azores, J.
    Climate, 25, 7381–7398, https://doi.org/10.1175/JCLI-D-11-00610.1, 2012.

Sandu, I., Brenguier, J., Geoffroy, O., Thouron, O., and Masson, V.: Aerosol impacts on the diurnal cycle of marine
    stratocumulus, J. Atmos. Sci., 65, 2705–2718, 2008.

Sandu, I., Brenguier, J.-L., Thouron, O., and Stevens, B.: How important is the vertical structure for the
    representation of aerosol impacts on the diurnal cycle of marine stratocumulus? Atmos. Chem. Phys., 9, 4039–
    4052, doi:10.5194/acp-9-4039-2009, 2009.

Sato, Y., Goto, D., Michibata, T., Suzuki, K., Takemura, T., Tomita, H., and Nakajima, T.: Aerosol effects on cloud
    water amounts were successfully simulated by a global cloud-system resolving model, Nat. Commun., 9, 985,
    https://doi.org/10.1038/s41467-018-03379-6, 2018.

Small, J., Chuang, P., Feingold, G. & Jiang, H.: Can aerosol decrease cloud lifetime? Geophys. Res. Lett. 36,
    L16806, 2009.

Stevens, B. and Feingold, G.: Untangling aerosol effects on clouds and precipitation in a buffered system, Nature,
    461, 607–613, doi:10.1038/nature08281, 2009.

Stevens, B. & Seifert, A.: Understanding the macrophysical outcomes of microphysical choices in simulations of
    shallow cumulus convection. J. Meteorol. Soc. Jpn 86A, 141–163, 2008.

Sun-Mack, S., Minnis, P., Chen, Y., Kato, S., Yi, Y., Gibson, S. C., et al.: Regional apparent boundary layer lapse
    rates determined from CALIPSO and MODIS data for cloud-height determination. Journal of Applied
    Meteorology and Climatology, 53(4), 990–1011, 2014.

Terai, C. R., Wood, R., Leon, D. C., and Zuidema, P.: Does precipitation susceptibility vary with increasing cloud thickness in marine stratocumulus? Atmos. Chem. Phys., 12, 4567–4583, doi:10.5194/acp-12-4567-2012, 2012.

Terai, C. R., Wood, R., and Kubar, T. L.: Satellite estimates of precipitation susceptibility in low-level marine stratiform clouds, J. Geophys. Res., 120, 8878–8889, doi:10.1002/2015JD023319, 2015.

Toll, V., Christensen, M., Quaas, J., and Bellouin, N.: Weak average liquid-cloud-water response to anthropogenic aerosols, Nature, 572, 51–55, https://doi.org/10.1038/s41586-019-1423-9, 2019.

Trepte, Q. Z., and Coauthors: Global cloud detection for CERES edition 4 using Terra and Aqua MODIS data. IEEE Trans. Geosci. Remote Sens., 57, 9410–9449, https://doi.org/10.1109/TGRS.2019.2926620, 2019.

Twomey, S.: The Influence of Pollution on the Shortwave Albedo of Clouds, J. Atmos. Sci., 34, 1149–1152, https://doi.org/10.1175/1520-0469(1977)034<1149:TIOPOT>2.0.CO;2, 1977.

Wang, S., Wang, Q., and Feingold, G.: Turbulence, Condensation, and Liquid Water Transport in Numerically Simulated Nonprecipitating Stratocumulus Clouds, J. Atmos. Sci., 60, 262–278, https://doi.org/10.1175/1520-0469(2003)060<0262:TCALWT>2.0.CO;2, 2003.

Wang, Y., Zheng, X., Dong, X., Xi, B.,Wu, P., Logan, T., and Yung, Y. L.: Impacts of long-range transport of aerosols on marineboundary-layer clouds in the eastern North Atlantic, Atmos. Chem. Phys., 20, 14741–14755, https://doi.org/10.5194/acp-20-14741-2020, 2020.

Warren, S. G., C. J. Hahn, J. London, R. M. Chervine, and R. L. Jenne: Global distribution of total cloud cover and cloud type amounts over ocean, Tech. Note NCAR/TN-317 + STR, 42, Natl. Cent. for Atmos. Res., Boulder, Colo., https://doi.org/10.2172/5415329, 1988.

Williams, A. S., & Igel, A. L.: Cloud top radiative cooling rate drives non-precipitating stratiform cloud responses to aerosol concentration. Geophysical Research Letters, 48, e2021GL094740. https://doi.org/10.1029/2021GL094740, 2021.

Wood, R.: Stratocumulus Clouds, Mon. Weather Rev., 140, 2373–2423, https://doi.org/10.1175/MWR-D-11-00121.1, 2012.

Wu, P., Dong, X., Xi, B., Tian, J., & Ward, D. M.: Profiles of MBL cloud and drizzle microphysical properties retrieved from ground-based observations and validated by aircraft in situ measurements over the Azores. Journal of Geophysical Research: Atmospheres, 125, e2019JD032205. https://doi.org/10.1029/2019JD032205, 2020.

Wu, P., X. Dong, and B. Xi: A climatology of marine boundary layer cloud and drizzle properties derived from ground-based observations over the Azores. J. Climate, 33, 10133–10148, https://doi.org/10.1175/JCLI-D-20-0272.1, 2020.

Xi, B., Dong, X., Minnis, P., & Khaiyer, M. M.: A 10 year climatology of cloud fraction and vertical distribution derived from both surface and GOES observations over the DOE ARM SPG site. *Journal of Geophysical Research*, *115*(D12). https://doi.org/10.1029/2009jd012800, 2010

Xue, H. and Feingold, G.: Large-Eddy Simulations of Trade Wind Cumuli: Investigation of Aerosol Indirect Effects, J. Atmos. Sci., 63, 1605–1622, https://doi.org/10.1175/JAS3706.1, 2006.

Yeom, J. M., Yum, S. S., Shaw, R. A., La, I., Wang, J., Lu, C., et al.: Vertical variations of cloud microphysical relationships in marine stratocumulus clouds observed during the ACE ENA campaign. Journal of Geophysical Research: Atmospheres, 126, e2021JD034700. https://doi.org/10.1029/2021JD034700, 2021.

Zhang, Z., Song, Q., Mechem, D. B., Larson, V. E., Wang, J., Liu, Y., Witte, M. K., Dong, X., and Wu, P.: Vertical dependence of horizontal variation of cloud microphysics: observations from the ACE-ENA field campaign and implications for warm-rain simulation in climate models, Atmos. Chem. Phys., 21, 3103–3121, https://doi.org/10.5194/acp-21-3103-2021, 2021.

Zhang, J., Zhou, X., Goren, T., and Feingold, G.: Albedo susceptibility of northeastern Pacific stratocumulus: the role of covarying meteorological conditions, Atmos. Chem. Phys., 22, 861–880, https://doi.org/10.5194/acp-22-861-2022, 2022.

Zhang, J., and Feingold, G.: Distinct regional meteorological influences on low-cloud albedo susceptibility over global marine stratocumulus regions, Atmos. Chem. Phys., 23, 1073–1090, https://doi.org/10.5194/acp-23-1073-2023, 2023.

Zheng, Q., and Miller, M. A.: Summertime Marine Boundary Layer Cloud, Thermodynamic, and Drizzle Morphology over the Eastern North Atlantic: A Four-Year Study, J. Climate, 35, 4805-4825, https://doi.org/10.1175/JCLI-D-21-0568.1, 2022.

Zheng, X. J., B. K. Xi, X. Q. Dong, P. Wu, T. Logan, and Y. Wang, 2022: Environmental effects on aerosol–cloud interaction in non-precipitating marine boundary layer (MBL) clouds over the eastern North Atlantic. Atmospheric Chemistry and Physics, 22, 335−354, https://doi.org/10.5194/acp-22-335-2022.

Zhou, X., Zhang, J., & Feingold, G.: On the importance of sea surface temperature for aerosol-induced brightening of marine clouds and implications for cloud feedback in a future warmer climate. Geophysical Research Letters, 48, e2021GL095896. https://doi org/10.1029/2021GL095896, 2021.

Zhou, X., & Feingold, G. (2023). Impacts of mesoscale cloud organization on aerosol-induced cloud water adjustment and cloud brightness. Geophysical Research Letters, 50, e2023GL103417. https://doi.org/10.1029/2023GL103417

Zuidema, P., Leon, D., Pazmany, A., & Cadeddu, M.: Aircraft millimeter-wave passive sensing of cloud liquid water and water vapor during VOCALS-REx. *Atmospheric Chemistry and Physics*, *12*(1), 355-369. https://doi.org/10.5194/acp-12-355-2012, 2012